In-situ Electrochemical Scanning

Transmission X-ray Microscopy (STXM)

Development of *in-situ* Flow

Electrochemical Scanning Transmission

X-ray Microscopy (STXM)

By

VINOD PRABU, B. Tech

A Thesis

Submitted to the School of Graduate Studies

in Partial Fulfillment of the Requirements

for the Degree

Master of Science

McMaster University

ii

MASTER OF SCIENCE (2017)   McMaster University

(Chemistry)   Hamilton, Ontario

TITLE: Development of *in-situ* Flow Electrochemical Scanning Transmission X-ray Microscopy (STXM).

AUTHOR: Vinod Prabu, B.Tech. (Anna University, Chennai)

SUPERVISOR: Professor A. P. Hitchcock

NUMBER OF PAGES: xx, 111

ABSTRACT

Understanding electrically activated processes at electrode-electrolyte interfaces is needed to improve many technologies, including energy conversion, semiconductor devices, bio-sensors, corrosion protection, etc. *In-situ* spectro-electrochemical studies based on a wide range of spectroscopies are particularly useful. Scanning Transmission X-ray microscopy (STXM) is a synchrotron-based technique which measures near-edge X-ray absorption fine structure (NEXAFS) with high spatial resolution. In addition to information on morphology, STXM also provides chemical state analysis using the X-ray absorption data, which makes *in-situ* STXM studies of electrochemical process of special interest. This thesis reports *ex-situ* and *in-situ* STXM based qualitative and quantitative studies on copper (Cu) electrodeposition and electrostripping. The influence of electrolyte pH on the distribution of Cu(I) and Cu(0) species electrodeposited from aqueous $CuSO_4$ solutions was studied. An instrument capable of performing *in-situ* <u>flow</u> electrochemical STXM studies was designed and fabricated. The performance of this device was evaluated for *in-situ* Cu electrodeposition studies. Findings based on *ex-situ* and *in-situ* STXM studies are discussed. Suggestions are made for further instrumentation improvements.

ACKNOWLEDGEMENTS

Firstly, I thank Dr. D. K. Pattanayak and Dr. G. Sreedhar, CSIR-CECRI, India for providing me the first motivation and opportunity to pursue scientific research, without which I might not have taken up graduate studies.

Special thanks to all of my labmates for the friendly environment in lab. Thanks to Dr. Scott Rosendahl who provided me the first orientation to the scope and feasibility of *in-situ* electrochemical STXM. I'm thankful to Dr. Jian Wang, Dr. Chitra Karunakaran, and Yingshen Lu (Canadian Light Source) & Dr. David Kilcoyne, Dr. Young-Sang Yu and Dr. David Shapiro (Advanced Light Source) for their support through the beamtime hours utilized for this project.

I thank Prof. Peter Kruse and Prof. Gillian Goward for serving as my M.Sc committee and for their interest in my project. Sincere Thanks to Prof. Martin Obst and Dr. Narayan Appathurai, who were always very friendly, supportive, and motivating throughout the course of this project.

I'm sincerely grateful to Prof. Adam Hitchcock for accepting me as a graduate student to work on this project. Adam had provided many helpful suggestions and guidance in the development of this work. This project initially experienced multiple instrumentation failures. But, Adam was always very encouraging and accommodative to schedule me on all the beamtime I had requested.

This thesis is dedicated to my parents, M. Bhuwaneswari and A. P. Prabu. They always inspire me to give my best at everything. They have always been unconditionally loving and supportive, both emotionally, and monetarily. They are always my first teachers of science. They had spent a huge amount of time with me, through my high school days to establish a strong foundation and knowledge in science. That foundation has been helpful to me through every phase of my undergraduate and graduate studies.

Vinod Prabu,

July 12, 2017

Table of Contents

List of Figures

List of Tables

List of Abbreviations

Acronym	-------------	*Abbreviation*
AAS	-------------	*Atomic Absorption Spectroscopy*
AES	-------------	*Atomic Emission Spectroscopy*
AFM	-------------	*Atomic Force Microscopy*
ALS	-------------	*Advanced Light Source*
ANSYS	-------------	*Analysis Systems*
ATR	-------------	*Attenuated Total Reflection Spectroscopy*
BM	-------------	*Bending Magnets*
CAD	-------------	*Computer Aided Drafting*
CE	-------------	*Counter Electrode*
CLS	-------------	*Canadian Light Source*
CS	-------------	*Central Stop*
CV	-------------	*Cyclic Voltammetry*
ECE	-------------	*Two Electrochemical Steps with intermediary Chemical Step*
EE	-------------	*Two Electrochemical Steps*
EPU	-------------	*Elliptically Polarizing Undulators*
ESR	-------------	*Electron Spin Resonance Spectroscopy*
ETFE	-------------	*Ethylene tetrafluoroethylene*
FT-IR	-------------	*Fourier Transform - Infrared Spectroscopy*

ID	-------------	*Insertion Devices*
I_L	-------------	*Limiting Current*
IR	-------------	*Infrared*
MEMS	-------------	*Microelectro-mechanical Systems*
NA	-------------	*Numerical Aperture*
NCF	-------------	*National Coarse/Fine*
NEXAFS	-------------	*Near Edge X-ray Absorption Fine Spectra*
NMR	-------------	*Nuclear Magnetic Resonance*
NSLS	-------------	*National Synchrotron Light Source*
OD	-------------	*Optical Density*
OSA	-------------	*Order Sorting Aperture*
PEM-FC	-------------	*Polymer Electrolyte Membrane - Fuel Cell*
PES	-------------	*Photo Electron Spectroscopy*
PMT	-------------	*Photomultiplier Tube*
PTFE	-------------	*Polytetrafluoroethylene*
RE	-------------	*Reference Electrode*
RGB	-------------	*Red-Green -Blue*
ROI	-------------	*Region of Interest*
SECM	-------------	*Scanning Electrochemical Microscopy*
SEM	-------------	*Scanning Electron Microscopy*

SM -------------- *Spectro-Microscopy*

SR -------------- *Synchrotron Radiation*

STM -------------- *Scanning Tunneling Microscopy*

STXM -------------- *Scanning Transmission X-ray Microscopy*

SVC -------------- *Small Volume Cell*

TEM -------------- *Transmission Electron Microscopy*

USB -------------- *Universal Serial Bus*

UVSOR -------------- *Ultraviolet Synchrotron Orbital Radiation*

UV-Vis -------------- *Ultraviolet-visible Spectroscopy*

VI -------------- *Voltage-Current*

WE -------------- *Working Electrode*

XHD -------------- *Xtreme High Definition*

ZP -------------- *Zone Plate*

CHAPTER 1.   INTRODUCTION

This chapter introduces electrochemical science and rationalizes the need for improved tools to understand electrochemical processes. In-situ and operando electrochemical spectroscopic and microscopic techniques are reviewed. The present understanding of copper electro-deposition and electro-stripping is summarized. The chapter concludes with an outline of the thesis content.

1.1 Electrochemistry and its importance

Electrochemistry is concerned with the transfer of electrons at the solution/electrode interface. Studies on electrochemistry were set for rapid growth after the invention of the first battery by Alessandro Volta in 1800, which was an alternating stack of copper and zinc disks separated by paper soaked in acid (Volta 1800). By 1835, Michael Faraday had defined the concepts of anode, cathode, electrode, electrolyte, anions, and cations, etc (Ciobanu, Wilburn et al. 2007). Since, then the advancement in human understanding of electrochemistry has led to many modern technologies, including batteries, fuel cells, solar cells, super capacitors, health monitoring devices, aesthetic finishing of materials, corrosion protection, etc, and still growing. This has been achieved through continual improvements in our understanding of electrochemistry, using a range of material characterization and analytical techniques.

My thesis research involves advancing soft X-ray scanning transmission microscopy (STXM) instrumentation and its applications to determinations of the chemical states and spatial distributions of electroactive materials and intermediates involved in electrochemical reactions. The goal was to develop techniques to measure electrochemical processes as they proceed, so-called *in-situ* studies. In brief, a device has been developed to perform *in-situ* investigations of electrochemical processes with flowing electrolyte using an analytical microscopy called soft X-ray scanning transmission microscopy (STXM). *Ex-situ* and *in-situ* electrochemical STXM studies were conducted on copper electro-deposition and electro-stripping as a model system to demonstrate the potential of this technique.

1.2 Importance of *in-situ* electrochemical studies

Many of the existing applications of electrochemistry are a result of charge separations and chemical reactions that occur at the interface of electrode and electrolyte. The evolution of the structure, chemistry and composition at these interfaces plays a key role in determining the performance of a technology. This has motivated research into electrochemical processes at interfaces and transport phenomena through the boundary layers. This field of research can be classified into **three streams.** Firstly, understanding the chemical state(s) of product(s) of electrochemical reactions. Secondly, understanding the composition of each state and their structural evolution in the interface region. Ex-situ studies can answer

only some of these questions; in some cases, there are intermediates involved
which cannot be isolated for post-process studies. Thus, the third stream of
electrochemical research involves in-depth understanding into formation of the
double layer or processes involving heterogeneous ion or electron transfers. This
requires *in-situ* spectroscopic and spectro-microscopic probes of electrochemical
events. The challenge addressed in this thesis is the development of adaptive
spectro-microscopic instrumentation to enable *in-situ* studies of such selective
information and to record them as they take place in an electrochemical system of
interest.

1.2.1 In-situ electrochemical spectroscopy techniques

Spectroscopy uses interactions of electromagnetic radiation with matter to
investigate static structure and dynamic processes. Spectroscopy can be broadly
classified into absorption, emission, and scattering studies at specific wavelengths
of electromagnetic radiation, which gives rise to techniques such as Atomic
Absorption Spectroscopy (AAS), Atomic Emission Spectroscopy (AES), Infrared
Spectroscopy (IR), Raman Spectroscopy, Fluorescence Spectroscopy,
Photoemission Spectroscopy, Ultraviolet-Visible Spectroscopy (UV-Vis), Near
Edge X-ray Absorption Fine Structure (NEXAFS) Spectroscopy, Photoelectron
Spectroscopy (PES), Nuclear Magnetic Resonance spectroscopy (NMR), etc.
Performing spectroscopy studies of an active electrode-electrolyte interface can

provide information about the interface species using spectroscopic transitions. Typically, spatially resolved spectroscopy combined with active potential or current control – so called Spectro-electrochemical microscopy – is needed for a detailed understanding. A range of spectroscopic devices coupled to electrochemical cells have been developed and, in some cases commercialized. Some of the established *in-situ* spectro-electrochemical methods are *in-situ* UV-VIS spectro-electrochemistry, to study optically differentiated charge carriers during redox transformation (Genies, Bidan et al. 1983, Kuwabata, Yoneyama et al. 1984); *in-situ* FT-IR and Raman spectroscopy to probe electrochemical changes in chemical bonds (Kato, Nishikawa et al. 1991, Neugebauer 1995); *in-situ* Electron Spin Resonance Spectroscopy (ESR) to probe changes in magnetic moments (Compton and Waller 1985, Zotti and Schiavon 1989); *in-situ* NMR spectroscopy for investigation and characterization of electro-organic reactions (Lapkowski and Geniés 1990, Geniès and Noël 1991); etc. Often, some of these *in-situ* techniques are used in combination with conventional electrochemical characterization techniques such as electrochemical impedance spectroscopy, and A.C conductance studies (Bard and Faulkner 2001).

1.2.2 In-situ electrochemical microscopy techniques

Despite the extensive information provided by *in-situ* spectroscopic techniques (Christensen, Hamnett et al. 1988, Kim, Collins et al. 1991, Hillman, Loveday et al. 1992, Bacskai, Inzelt et al. 1994, Lankinen, Sundholm et al. 1998), there are cases where lateral spatial resolution is required, such as studies on nucleation of electrodeposits (Grogan, Bau et al. 2012), electro-kinetic studies (Grogan, Rotkina et al. 2011), etc. This is where *in-situ* surface sensitive microscopy techniques combined with electrochemical control come into use. These include Atomic Force Microscopy (AFM) (Bertrand, Rocca et al. 2000), Scanning Tunneling microscopy (STM)(Breuer, Funtikov et al. 1995), Scanning Electrochemical microscopy (SECM) (Souto, González-García et al. 2012), Scanning Electron Microscopy (SEM) (Arimoto , Oyamatsu et al. 2008) and Transmission Electron Microscopy (TEM) (Grogan and Bau 2010). These microscopy techniques, some of which can achieve atomic resolution, can be used to address questions related to dynamics of an electrochemical process.

1.2.3 In-situ electrochemical spectro-microscopy techniques

Electrochemical spectro-microscopy (imaging with spectral information) provides spatially resolved spectroscopy with active control of an electrochemical system. There are two approaches to achieve spectro-microscopy, One, combines electrochemistry, spectroscopy and microscopy methods (measuring/monitoring

two different physical phenomena) such as a combined SECM-Infrared Attenuated Total Reflection Spectroscopy (SECM & FT-IR-ATR) which is used to measure IR spectra during electrodeposition induced by feedback mode SECM (Wang, Kowalik et al. 2010). The second uses exclusive spectro-microscopy techniques (based only on transmission and absorption of electromagnetic radiation). Methods in this area includes scanning photoelectron spectro-microscopy, where chemically sensitive imaging based on core level photoionization is applied *in-situ* to an electrochemical process (Bozzini, Amati et al. 2012, Bozzini, Amati et al. 2013), and Scanning Transmission X-ray Microscopy (STXM), which can be used to perform chemical imaging based on NEXAFS spectroscopy to obtain chemical speciation (e.g. oxidation states) *in-situ* as an electrochemical reaction proceeds (Guay, Stewart-Ornstein et al. 2005, Hitchcock, Qin et al. 2016). The first demonstration of *in-situ* electrochemical STXM in soft X-ray range was published by Guay et. al. in 2005. Since then many other studies have been reported (Jiang, Chen et al. 2010, Bozzini, Mele et al. 2011, Gianoncelli, Kaulich et al. 2011, Bozzini, Amati et al. 2012, Bozzini, Gianoncelli et al. 2013, Gorlin, Lassalle-Kaiser et al. 2013). Recently there has been progress in this field toward performing *in-situ* <u>flow</u> electrochemical studies in a STXM (Nagasaka, Hatsui et al. 2010, Bozzini, Gianoncelli et al. 2014, Lim, Li et al. 2016). A detailed description of STXM is provided in the next chapter. The research presented in this thesis focuses on development of a flow

electrochemical cell for STXM, designed and fabricated in collaboration with Norcada Inc, (a MEMS fabrication company), followed by demonstration of the technique using *in-situ* monitoring of copper electrodeposition as a model system.

1.3 Electrochemical techniques & Copper electrochemistry

1.3.1 Electrochemical techniques

Electrochemistry studies electron transfer processes. This section outlines key electrochemical techniques used to characterize the reduction-oxidation (redox) properties of a material or system. Classical experiments in electrochemistry include potential step, potential sweep, sweep and step combinations, and alternating current (A.C) impedance techniques. In this thesis, potential step and potential sweep techniques are used to understand electrochemical deposition and stripping at gold (Au) surface. A more detailed description of electrochemical techniques can be found elsewhere (Bard and Faulkner 2001).

Figure 1.1a presents the typical current response when a constant step potential is applied at an electrode-electrolyte interface. If an electrode (A) is initially maintained at a constant potential V_1, at which no electrochemical event occurs, the concentration of electroactive species (O) at the surface of the electrode is zero and any mass transfer at the electrode surface is due to diffusion of O from the bulk to the electrode due to existing concentration gradients at the double layer.
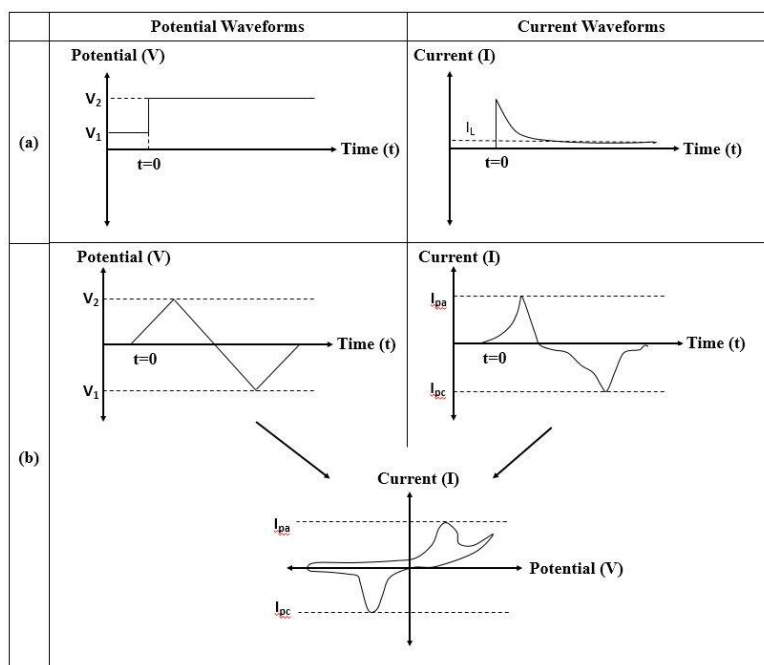
Figure 1.1 Typical Current Responses for (a) Potential Step, and (b) Potential

Sweep Voltammetry experiments.

If at time t=0 the electrode is brought to potential V_2 a sudden spike is observed

followed by saturation at a constant limiting current (I_L) where mass transport

controlled reduction of O dominates, [O + e- → R], similarly oxidation of R

dominates, [R → O + e$^-$] when corresponding reverse potential is applied and O is

regenerated. The spike observed is referred to as the IR drop at the interface

caused by formation of double layer charge (John, Reddy et al. 2001), which is

8

defined as the charge required to overcome the double layer potential at the electrode-electrolyte interface.

Figure 1.1b represents a typical current response when the electrode potential is changed linearly with time between two chosen values E_1 and E_2, as is used in potential step methods. There are two types of potential sweep techniques; linear sweep and cyclic sweep, with the latter called cyclic voltammetry (CV). CV is traditionally used to understand the reaction mechanisms in an electrochemical system. The applied potential waveform of a CV scan is represented in **Figure 1b**, keeping in mind that a potential step waveform changes the electrode potential, produces new surface concentrations for O and R, and induces diffusion between the bulk and the electrode surface. From Fick's first law of diffusion (Bard and Faulkner 2001), the current response will be proportional to the gradient of concentration from the electrode surface to the bulk of the electrolytic solution. **Figure 1.2** represents the cyclic voltammogram for a diffusion-controlled electron transfer process at an electrode and the concentration profiles along the surface of electrode at points 1-10 on the CV curve. For points 1-7, species O is consumed at the electrode and a reduction current is observed. For points 8-10, O is regenerated by oxidation of R and an oxidation current is observed. It is to be noted that the change of direction in current is directly related to the inversion of the concentration gradient of O at the electrode surface; the gradient is positive for points 1-7, and is negative for points 8-10. More information on equations

governing the current responses and advanced interpretation of CV technique can

be found in (Digby 1977).
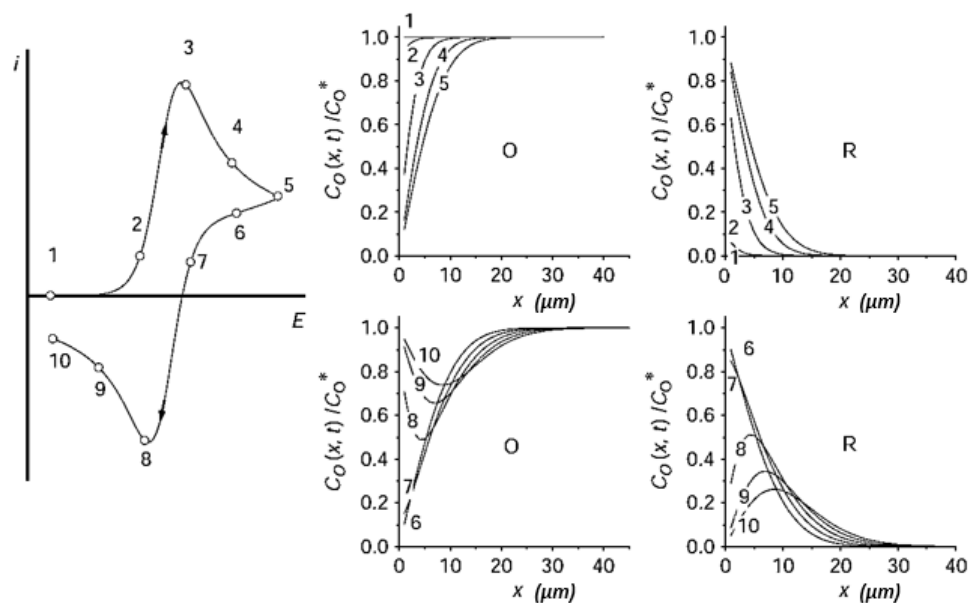
Figure 1.2 Cyclic voltammogram and corresponding O and R concentration

profiles for diffusion to a planar electrode. (Numbers on the concentration

profiles correspond to the numbered points on the voltammogram.) adapted

(Ciobanu, Wilburn et al. 2007) with permissions from Elsevier.

1.3.2 Copper electrochemistry

Copper (Cu) metal has high thermal & electrical conductivity, and resistance to galvanic corrosion. It is often used as an electrical conductor due to its exceptional conductivity and reasonable cost (Morehouse and Burris 1978). Apart from traditional electrical wires, copper and its species are used in semiconductor integrated circuits, printed circuit boards (PCB's), solar cells (Rahman, Islam et al. 2015), and metal finishing. Chemically, copper is a material with virtually 100% recyclability which is done through refining (acid dissolution and precipitation) and/or through electrowinning (electro-reduction) from acid solutions. Before discussing electro-reduction and electro-oxidation steps of copper, it is important to understand the standard redox potentials of copper under equilibrium conditions at its electrode (copper) - electrolyte (aqueous solution of cupric ions) interface. This can be determined by a variety of approaches, such as

$$
\begin{array}{c}
E_{2\text{-}0} \\
\underline{\hspace{0.5cm} 0.340\ V \hspace{0.5cm}} \\
Cu^{2+} \xleftarrow{\ 0.159\ V\ } Cu^{1+} \xleftarrow{\ 0.520\ V\ } Cu^{0} \\
2 \qquad E_{2\text{-}1} \qquad 1 \qquad E_{1\text{-}0} \qquad 0
\end{array}
$$
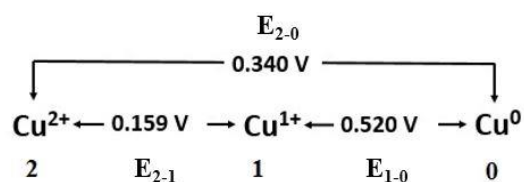
Figure 1.3 Standard redox potential diagram of copper electrochemical system [Half-cell potentials under reversible conditions w.r.t. Standard hydrogen Electrode (SHE)]

redox titrations, cyclic voltammetry, potentiostatic methods involving spectral

monitoring, and pulsed methods.

Figure 1.3 presents the standard redox potentials between the states of

cupric and cuprous ions in water and Cu metal (Bard, Parsons et al. 1985). It can

be noted that, in water $E_{1-0} > E_{2-1}$, which means solvated Cu(I) is unstable

according to the disproportionation;

$$2Cu^+ \text{ (aq)} \Leftrightarrow Cu^{2+} \text{ (aq)} + Cu \text{ (s)} \qquad K_{disp} = \frac{[Cu^{2+}]}{[Cu^{1+}]} \qquad \textbf{(Eqn. 1.1)}$$
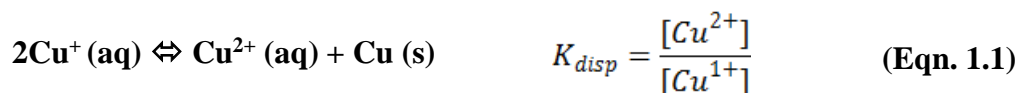
The K_{disp} for water at pH = 7.0 is 1.7×10^6 which is relatively large, although there

is a finite amount of Cu(I) in any Cu(II) solution in contact with solid copper. In

water, the disproportionation equilibrium (eqn. 1.1) implies that the fraction of

Cu(I) with respect to Cu(II) in solution increases as the concentration of Cu ions

decreases. So, at micromolar (μM) concentrations in water, the two oxidation

states can even be maintained in equal amounts. This is the reason that trace

amounts of Cu(I) species are found in copper electroplating systems (Danilov,

Molodkina et al. 2005). This unwanted effect is minimized by adding millimolar

(mM) concentrations of chloride (Cl⁻) to the plating bath as additives, which

stabilizes the Cu(I) ions in the vicinity of the electrode surface and reduces the

potential barrier (IR drop) in the system (Soares, Wasle et al. 2002). This results

in an improved efficiency of the electrodeposition process due to consumption of

lower current. There are some areas in which it is desirable to have Cu(I) electrodeposition such as dye sensitized solar cells (as photo-anode dopants) (Horng-Show, Der-Tsuey et al. 2012). In these cases, electrodeposition is carried out in an alkaline electrolyte in the presence of complexing agents (Rahman, Islam et al. 2015). It is also claimed that improved stabilization of Cu(I) species can be achieved in acidic electrolytes by carrying out electro-reduction at intermediate pH between 2 - 3.5 (Danilov, Molodkina et al. 2005). The research work in this thesis attempts to evaluate this claim through qualitative and quantitative measurements of the distributions of Cu(I) and Cu(0) species formed in *ex-situ* investigations, and *in-situ* electrodeposition studied by STXM.

1.4 Outline of this thesis

Chapter 2 outlines the principles of synchrotron radiation, near edge X-ray absorption fine structure spectroscopy (NEXAFS), scanning transmission X-ray microscopy (STXM) and the ALS 5.3.2.2 polymer STXM and CLS 10ID1 ambient STXM, as well as their beamlines. It also describes the electrochemical apparatus and techniques used at McMaster University to study Cu electro-deposition and electro-stripping, and to prepare *ex-situ* samples for STXM characterization.

Chapter 3 describes STXM studies of samples of Cu *ex-situ* electrodeposited on Au from an acidic electrolyte, which were carried out to

investigate the influence of pH on the distribution of Cu(I) and Cu(0) in the electrodeposits. Sample preparation procedures for pure reference compounds and *ex-situ* samples are described. Measurement of NEXAFS reference spectra of Cu(0), Cu(I) and Cu(II) states of copper are outlined. Methods for qualitative and quantitative analysis of electrodeposits are described. Finally, the findings from STXM studies of electrodeposits prepared *ex-situ* from electrolytes of different pH are reported.

Chapter 4 describes the design and features of the *in-situ* electrochemical flow cell used in this research. It discusses the spatial constraints imposed by STXM on the holder design and summarizes various stages of holder design which have evolved to the existing Phase 1b holder. Finally, it concludes with a step-by-step guide to assembly of the flow cell.

Chapter 5 presents results of an *in-situ* study of Cu electro-deposition and electro-stripping. It discusses optimum design of *in-situ* electro-chemical STXM experiments, describes data collection and interpretation methods, and presents key findings on the Cu system based on the *in-situ* data.

Chapter 6 summarizes the improvements achieved in *in-situ* flow electrochemical STXM and what was learnt from the *ex-situ* STXM studies of Cu electrodeposition. The present shortcomings of this instrument and proposals for future work to advance this technique are discussed.

CHAPTER 2.   METHODS

This chapter outlines the principles of synchrotron radiation, near edge X-ray absorption fine structure spectroscopy (NEXAFS), scanning transmission X-ray microscopy (STXM) and the ALS 5.3.2.2 polymer STXM and CLS 10ID1 ambient STXM, as well as their beamlines. It also describes the electrochemical apparatus and techniques used at McMaster University to study Cu electro-deposition and electro-stripping, and to prepare e-situ samples for STXM characterization.

2.1 Synchrotron radiation

When a charged particle is accelerated electromagnetic radiation is generated (Williams 1982). This is exploited in generation of synchrotron radiation (SR), where charges, usually electrons, traveling at a fixed speed close to the speed of light, are accelerated by being forced to move on a curved path by external magnetic fields. Synchrotron radiation facilities are accelerator systems which produce a wide range of electromagnetic radiation from the synchrotron effect. A synchrotron radiation facility consists of an electron (in some cases, positron) source, an initial accelerator (microtron or linear accelerator), a booster synchrotron ring, and the storage ring where the light is produced. **Figure 2.1** is a sketch of a typical facility. The booster ring is a set of electromagnets which provide variable field strength used to accelerate the electrons from that of the

source and initial accelerator, to that of the storage ring. The magnetic field in the

booster ring bend magnets is raised synchronously with the particle energy (which

is the origin of the term synchrotron) to keep the electrons on a circular path with

a constant radius.
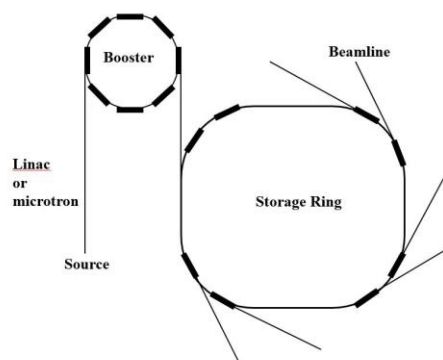
Figure 2.1 Schematic of a Synchrotron Facility. [adapted from (Hahner 2006), with permissions from Royal Society of Chemistry.]

When the electrons have reached the desired relativistic energy, they are

transferred to the storage ring, where the magnetic field in the curved sections

('bend magnets') remains constant. The electrons then orbit in the storage ring.

Synchrotron radiation is generated in bending magnets (BM, keeping the electrons

on a closed path), and in insertion devices (ID) such as wigglers or undulators that

are placed in linear sections of the storage ring (Mobilio, Boscherini et al. 2015).

Synchrotron radiation covers a wide range of the electromagnetic spectrum, which

depends on the energy of the stored electrons and the nature of the source point

(BM or ID), and hence differ for the different synchrotron sources around the world. In the X-ray range (>100 eV) the flux (photons per second) is superior to conventional sources by orders of magnitude. Perhaps more important for STXM (which uses a circular diffractive optic for focusing that works most effectively with coherent light), is the brightness, which is the flux per unit source size and per unit solid angle per photon energy interval, typically in units of photons per second per milliradian^2 per mm^2 per 0.1% energy bandwidth (Mills, Helliwell et al. 2005).

X-rays emitted by the source point of the storage ring (BM or ID) are conveyed to experimental end stations such as a STXM microscope through beamlines, which contain mirrors to focus and steer the X-rays and a monochromator to disperse the spectrum of X-rays from which a single photon energy is selected by an exit slit. In addition to high brilliance, synchrotron light is highly polarized (Mobilio, Boscherini et al. 2015). Bend magnet sources produce X-rays which are linearly polarized in the plane of the storage ring. Linear undulators also produce horizontal linear polarized light. Elliptically polarizing undulators (EPU), such as the source point for the spectro-microscopy (SM) beamline 10ID1 at the Canadian Light Source (CLS), have mechanically adjustable magnet arrays which provide pure left and right circular polarized light as well as pure linear polarized light for which the E-vector can be re-oriented. The CLS-SM EPU is the most flexible ID of any STXM beamline since it can

adjust the E-vector orientation over 180º range (±90º relative to horizontal). The ability to select the E-vector orientation relative to the sample orientation is very useful for NEXAFS spectro-microscopy studies of anisotropic materials.

2.1.1 Near Edge X-ray Absorption Fine Structure (NEXAFS) spectroscopy

NEXAFS probes the excitation of core electrons into unoccupied bound or continuum states, through the absorption of electromagnetic radiation. The resulting core hole is then filled through the Auger process or by an electron from a valence shell, along with emission of an X-ray fluorescent photon. NEXAFS spectra can be recorded by measuring the transmitted photons, emitted electrons, Auger electrons, X-ray fluorescent photons, luminescent photons, or a combination of them. In this thesis, the NEXAFS spectra (Stöhr 1992) were all recorded by measuring the photons transmitted through samples (and subsequently applying the Beer-Lambert law). Absorption edges of different elements are generally well separated in energy so that they can be studied independently.

The X-ray absorption cross section (σ_x), is defined as the number of photons absorbed per unit time divided by the number of incident photons per unit time per unit area (Stöhr 1992). The measured cross-section can be related to the electronic states and transition probabilities predicted by quantum mechanics by:

$$\sigma_x = \frac{P_{if}(E)}{F_{ph}(E)} \qquad \text{(eqn 2.1)}$$

where, $F_{ph}(E)$ is the number of photons per unit time per unit area given by the energy flux of electromagnetic field divided by the photon energy, $P_{if}(E)$ is the transition probability which describes a transition from an initial state Ψ_i to a final state, Ψ_f induced by a time dependent electric field perturbation, ($V(t) = V_0 e^{-i\omega t}$) and can be expressed within the Fermi golden rule approach as: (Stöhr 1992)

$$P_{if}(E) = \frac{2\pi}{\hbar} \left| \langle \Psi_f | V(E,t) | \Psi_i \rangle \right|^2 \rho_f(E) \qquad \text{(eqn 2.2)}$$

where, $\rho_f(E)$ is the energy density of the final states. The X-ray absorption cross section is obtained by evaluating V(E,t) within the electric dipole approximation (Stöhr 1992):

$$\sigma_x(E) = \frac{4\pi^2 e^2}{m^2 c \omega} \left| \langle \Psi_f | e \cdot p | \Psi_i \rangle \right|^2 \rho_f(E) \qquad \text{(eqn 2.3)}$$

where, e and m, are the charge and mass of an electron, respectively; ω, is the angular frequency of the electromagnetic wave, and c is the speed of light; e is the unit potential vector and p is the sum of the linear momentum operators of the electrons. The optical oscillator strength (f_{osc}) is a parameter related to the X-ray

absorption cross section and used in spectroscopy to express the intensity of

electronic transitions (Stöhr 1992):

$$f_{osc} = \frac{2}{m\hbar\omega}|\langle\Psi_f|e\cdot\wp|\Psi_i\rangle|^2 \qquad \textbf{(eqn 2.4)}$$

2.2 Scanning Transmission X-ray Microscopy (STXM)

2.2.1 Principles of STXM

In STXM, soft X-rays produced by a bend magnet or an undulator are

monochromated and focused by a Fresnel zone plate (ZP) to a 20-50 nm spot

(Howells, Jacobsen et al. 2007). The sample is placed at the focal point of the ZP.
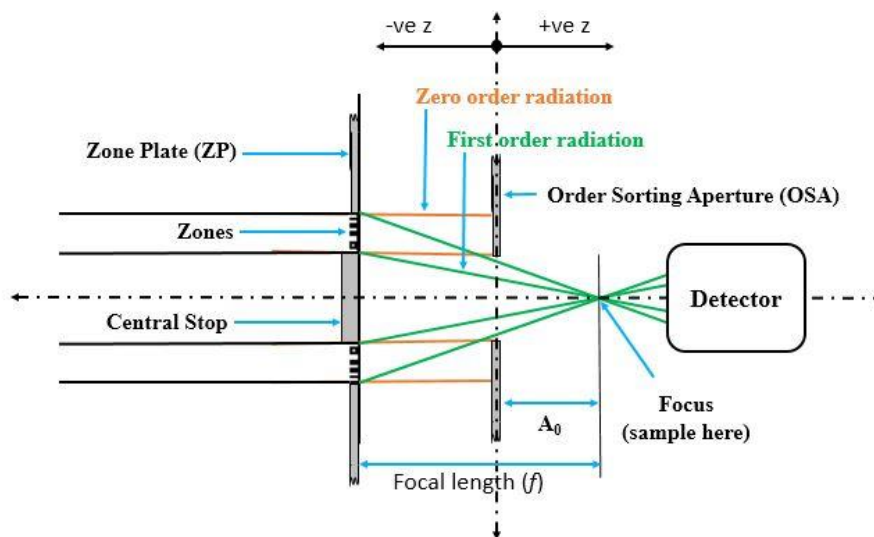
Figure 2.2 Key optical

Images are generated by (x, y)-raster scanning the sample while the transmitted

X-ray intensity (I) is recorded. The optical density (OD) is derived from (I) using

the Beer and Lambert law (Lambert 1760). The OD is related to the transmission

properties of the sample by (Hitchcock 2012):

$$OD = \ln\left(\frac{I_0}{I}\right) = \mu(E) \cdot \rho \cdot t \qquad \text{eqn. 2.5}$$

where, I_0 is the incident X-ray flux, I is the transmitted X-ray flux through the

sample, $\mu(E)$ is the mass absorption coefficient at X-ray energy E, ρ is the density,

and t is the thickness of sample.

Figure 2.2 presents a sketch of the key optical components of a STXM. A

zone plate (ZP) is a circular diffraction grating capable of focusing light. ZPs

consists of a series of alternating concentric rings of Au or Ni (thick enough to be

opaque to soft X-rays), and circular light transparent slots patterned on a silicon

nitride substrate. The interference condition of this structure is described by:

$$r_n^2 = nm\lambda f + \frac{n^2 m^2 \lambda^2}{4} \qquad \text{(eqn 2.6)}$$

where f is the focal length, r_n is the radius of the nth zone, n is the zone number, m

is diffraction order, and λ is the wavelength of the incident soft X-ray. The zero-

diffraction order is un-diffracted light, and positive orders are converging light.

When adjacent transparent and opaque slots have equal width, the even-numbered orders are suppressed and the remaining odd-numbered orders interfere constructively at the focal point (Attwood 2007). The first order light which is the most intense diffracted light (~10% of the total flux), is used in most STXM measurements (Kilcoyne, Tyliszczak et al. 2003). An order sorting aperture (OSA) and a central stop (CS) in the center of the ZP with a diameter bigger than that of the OSA are used to block zero order and minimize higher order diffracted light. For first order diffraction ($m = 1$), the focal length (f) is given by:

$$f \approx \frac{r_n^2}{\lambda}$$
(eqn 2.7)

The numerical aperture (NA) of a ZP is given by (Attwood 2007):

$$NA = \frac{r_n}{f} = \frac{\lambda}{2\Delta r_n}$$
(eqn 2.8)

For a ZP with 'n' zones, n can be calculated from the radius of the outmost zone, r_n whose width is $\Delta r_n = r_n \ r_{n-1}$.

The focal length (in μm) is thus given by:

$$f = \frac{2r_n \Delta r_n}{\lambda} = \frac{D \Delta r_n E}{1240}$$
(eqn 2.9)

where, $D = 2r_n$, is the diameter of the zone plate in μm, E is photon energy in eV and Δr_n is given in nm. The focal length is inversely proportional to the wavelength of the light, and thus linearly proportional to the photon energy. The spatial resolution of a ZP can be expressed by the Rayleigh criterion (Howells, Jacobsen et al. 2007);

$$Resolution, \Delta r \ = \frac{0.610\lambda}{NA} = 1.22\Delta r_n \qquad \textbf{(eqn 2.10)}$$

Thus, the outer zone width of a zone plate determines the diffraction-limited spatial resolution.

2.2.2   STXM instrumentation

The first soft X-ray STXM was developed on the low energy ring at the National Synchrotron Light Source (NSLS-1) NY, USA (Janos and Harvey 1985), which used a 1 μm diameter pinhole as a scanning probe to image wet biological samples. The use of ZP and synchrotron radiation produced by an undulator in STXM began in late 1980's (Rarback, Shu et al. 1988, Buckley, Rarback et al. 1989). In 2001, an interferometer controlled STXM was built on a dedicated bend magnet beamline 5.3.2.2 at the ALS (Warwick, Ade et al. 2002, Kilcoyne, Tyliszczak et al. 2003). Although there was an earlier effort at using interferometry to improve the fidelity of imaging at the NSLS UV ring (Rarback, Shu et al. 1988), the implementation of interferometer-control at the 5.3.2.2

STXM ("polymer-STXM') is widely recognized as a major breakthrough in the development of STXM.

STXM microscopes at beamline 5.3.2.2 at the ALS and 10ID1 at the CLS were used for all analytical measurements reported in this thesis. These microscopes are quite similar. The external appearance of these microscopes is shown in **Figure 2.3**. The vacuum chambers and all the microscope components were designed to operate in air or at a vacuum of ~10^{-2} torr. Typically, measurements are performed with the chamber evacuated and backfilled with Helium (He) to a pressure of 250 torr (ALS 5.3.2.2 STXM) or 130 torr (CLS a-STXM). He is soft X-ray transparent, and has high thermal conductivity so it helps cool the motors, stages, and avoid thermal gradients (Kilcoyne, Tyliszczak et al. 2003). In addition, the absence of oxygen significantly reduces radiation
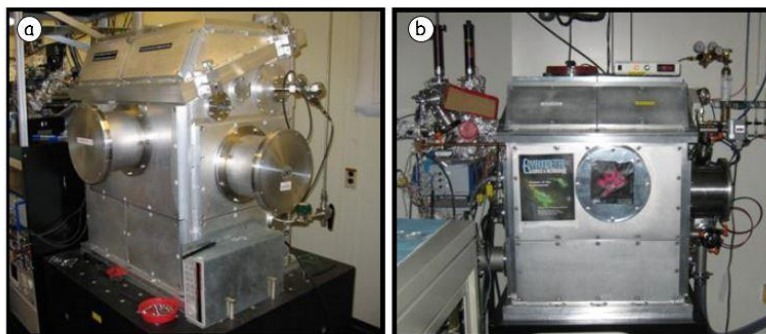
Figure 2.3 The STXM microscopes at (a) polymer-STXM ALS 5.3.2.2 and (b) a-STXM CLS 10ID1.

damage (Coffey, Urquhart et al. 2002).

The microscopes are mounted on massive granite blocks, which sit on vibration isolation pads to reduce vibrational coupling to the experimental floor. The central stop of the ZP has a diameter of 80-100 μm while the order sorting aperture (OSA) is typically 50 μm in diameter. The STXM sample plate has six 2.8 mm diameter round holes, designed to hold TEM grids or silicon nitride windows. In the ALS 5.3.2.2 STXM, only 5 of the holes can be used since moving to position #1 causes collisions between the sample support structure and the detector support structure; however, in the CLS a-STXM samples can be mounted on all six holes.

The ZP and sample must maintain relative (*x, y*) positioning accuracy of
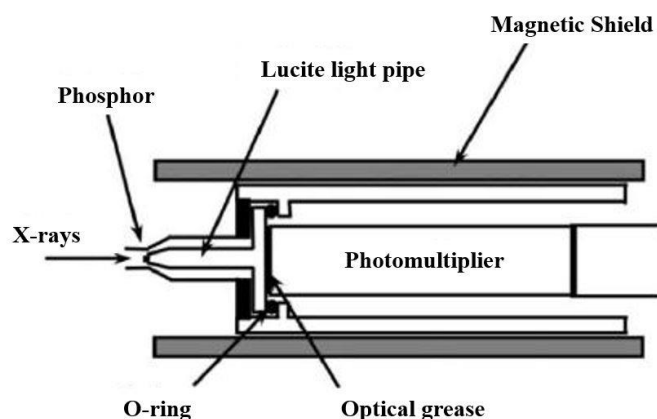
Figure 2.4 Schematic diagram of the X-ray detector in the STXM which includes a phosphor screen and a photomultiplier tube. [adapted from (Kilcoyne, Tyliszczak et al. 2003)]

10 nm (or better) between the ZP and sample. This is achieved by a laser interferometer control system (Kilcoyne, Tyliszczak et al. 2003). The interferometric system corrects for small drifts during acquisition of stacks of images.

The detector consists of a phosphor to convert soft X-rays to visible light followed by a high-performance photomultiplier (PMT) (Kilcoyne, Tyliszczak et al. 2003) which can count linearly up to 20 MHz (**Figure 2.4**). A very thin layer of a polycrystalline phosphor film (P43) is deposited on the lightly greased tip of a Lucite pipe to form the X-ray detector.

2.3 Lab-based electrochemical instrumentation and methods

Potential step and potential sweep techniques are used in this work to investigate Cu electrochemical system and to perform *ex-situ* & *in-situ* studies on Cu electro-deposition and electro-stripping. An Ivium pocketSTAT potentiostat (Ivium Technologies) was used. This is a USB powered/controlled potentiostat capable of performing experiments up to a scan range of $\pm$4V (0.2%) and $\pm$10mA (0.2%), and possessing a current resolution of <0.15 pA and a potential resolution of <16nV, when used in combination with IviumSoft^{TM} software (Ivium Technologies). The PocketStat is compatible with Windows XP/7/8/10. It can be used in two setups; namely, two-electrode systems (counter electrode and working electrode) or three-electrode systems (counter electrode, working electrode and

reference electrode). **Figure 2.5** presents a photograph of the potentiostat set up with a three-electrode cell.

The electrochemical cell set up presented in **figure 2.5** is a *Bio-Logic Small Volume Cell-3 (SVC-3)* (BioLogic), which is a small voltammetry cell designed for applications requiring only a small volume of electrolyte. It can be used with counter electrode (CE), working electrode (WE) and reference electrode (RE) with a diameter of 6 mm, which can be mounted on a polytetrafluoroethylene (PTFE) cap provided with SVC-3 and supports electrolyte volumes from 5 mL to 20 mL. **Figure 2.6** represents a photograph of the cell set-
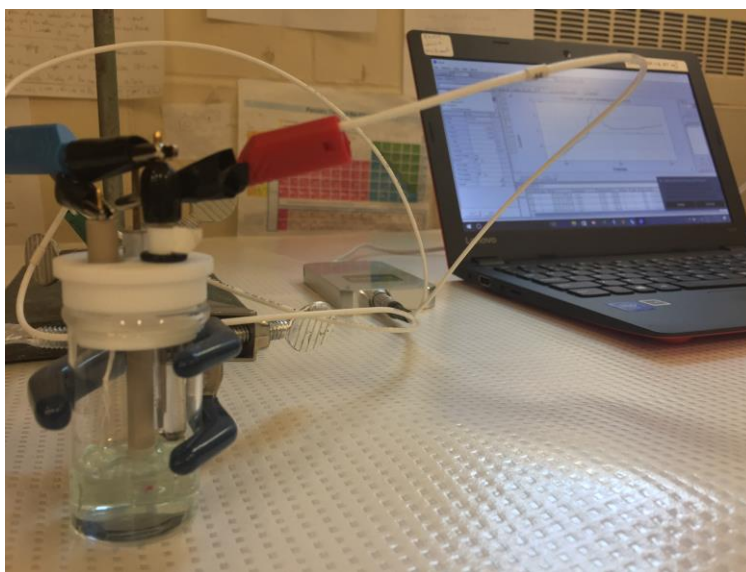
Figure 2.5 Photograph of Ivium pocketSTAT: galvanostat setup with a three-electrode cell.
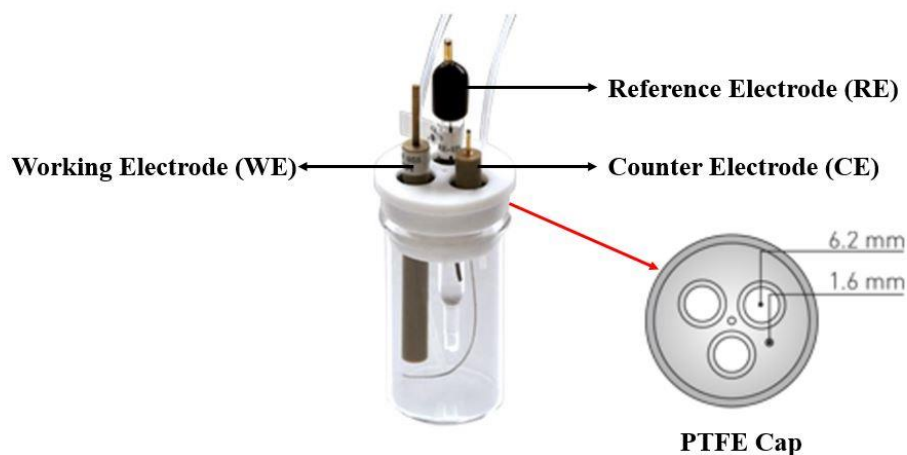
Figure 2.6 Photograph of SVC-3 electrochemical cell set-up and the PTFE cap to mount the electrode.

up with 3-electrodes (CE, WE and RE) and the PTFE cap used to mount the electrodes.

An electrochemical workstation combining Ivium and BioLogic equipment has been used throughout this work for all *ex-situ* sample preparation and benchtop studies on Cu electrochemical system. The electrolytes (to be discussed in detail in chapter 3) were all freshly prepared before each experiment for *ex-situ* studies. Ideally, electrolytes should be degassed by bubbling Nitrogen or Argon through the electrolyte in a closed cell. However, in the experiments involved in this work, the *ex-situ* electrolyte was used as freshly prepared, to mimic the cell and electrolyte conditions used for *in-situ* studies where degassing

could not be performed due to the spatial constraints of the micro flow cell device
(see **chapter 4**).

Figure 2.7 represents a screenshot from the IviumSoft^{TM} software used in
all the experiments conducted in this research. The cyclic voltammetric response
in the screenshot is from one of the CV experiments conducted on the Cu
electrochemical system at pH=2.0. In **figure 2.7,** *pane 1* lists the types of
electrochemical techniques that can be performed with the device with the CV and
Transient techniques expanded in detail (most used in this work). ***Pane 2*** is the
area where the intended experiment is designed. It has provisions to set the start
and stop potential values followed by the sweep rate and the potential or current
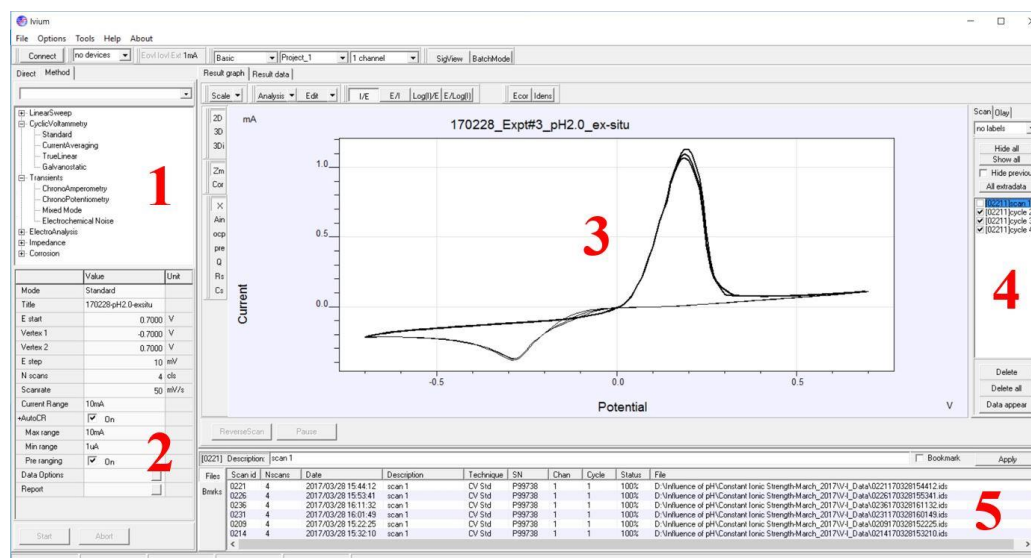
Figure 2.7 Screenshot of the Graphical User Interface (GUI) of the
IviumSoft^{TM}. Numbers (bold, red) indicate the most accessed panes in the GUI.

range setup for the instrument. The V and I ranges are selected to be appropriate to the system under study to provide sufficient sensitivity without overloading the amplifier. It is to be noted that there is an auto-scale feature for both V and I, but it was not used because changes in the amplifier scales cause discontinuity in the resulting data. *Pane 3* is the area where the VI-response is plotted as while the experiment is in progress and also has features to perform post-experiment processing, a detailed description of which can be found elsewhere (Ivium Technologies 2017). *Pane 4* provides the list of cycles in the case of a multiple cycle experiment, and *Pane 5* provides quick access to recently conducted experiments.

CHAPTER 3.   INFLUENCE OF pH ON Cu ELECTROCHEMISTRY

This chapter reports STXM studies of ex-situ samples of Cu electrodeposited on Au from an acidic electrolyte, which were carried out to investigate the influence of pH on the distribution of Cu(I) and Cu(0) in the electrodeposits. Sample preparation procedures for pure reference compounds and ex-situ samples are described. Measurement of NEXAFS reference spectra of Cu(0), Cu(I) and Cu(II) states of copper are outlined. Methods for qualitative and quantitative analysis of electrodeposits are described. Finally, the findings from STXM studies of electrodeposits prepared ex-situ from electrolytes of different pH are reported.

3.1 Introduction

Cuprous oxide (Cu_2O) electrodeposition is generally carried out in non-aqueous alkaline media with use of organic complexing agents as additives (de Jongh, Vanmaekelbergh et al. 1999, Rahman, Islam et al. 2015, Hossain, Al-Gaashani et al. 2017). There have also been reports claiming deposition of p-type and n-type Cu2O thin films from mildly acidic media using acetate complexing agents (Zhao, Fu et al. 2011, Wang, Wu et al. 2015). An improved stabilization of Cu(I) species in acidic aqueous electrolytes, has been reported at an intermediate acidic pH range of 2-3.5 (Danilov, Molodkina et al. 2005), brought about by OH⁻ adsorption at the electrode surface. As part of my research, STXM was used to

perform quantitative studies on *ex-situ* electrodeposited samples from aqueous electrolytes in the pH range of 1 – 4.5 in 0.5 unit pH increments. This study also serves to outline standard STXM data analysis methods used to extract quantitative speciation information about electrodeposited materials. Similar methods were used to analyze results from *in-situ* studies.

3.2 Design of two-electrode silicon chips

Soft X-ray spectro-microscopy studies of Cu electrodeposition were performed using custom fabricated silicon chips with X-ray transparent silicon nitride (Si_3N_4) windows on which Au electrodes were deposited (Norcada). **Figure 3.1** is a CAD model of two-electrode silicon chips used in all the *ex-situ* studies; the inset is a magnified view of the window region.
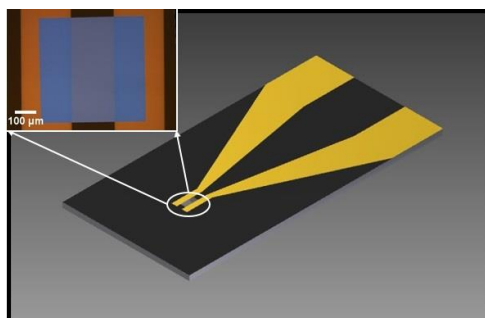
Figure 3.1 CAD model of two electrode silicon chip. <u>*inset*</u> – closer

view at the window region.

The 2-electrode chip is 10 mm x 5 mm with a 75nm thick, 500 μm x 500 μm Si_3N_4 window offset towards the bottom of the chip. Two parallel 20 nm thick gold (Au) electrodes, with chromium (Cr) adhesion layer are deposited on the chip surface which extend over the window region, creating two 150 μm x 500 μm sized electrode pads on the window for electrodeposition of materials (**inset, Figure 3.1**). These chips are mounted on a 5 x 2 cm Delrin plate and electrode clips are attached to carry out *ex-situ* deposition.

3.3 Experimental

3.3.1 Preparation of samples for reference NEXAFS spectra

The reference spectra for Cu(I) and Cu(II) species were extracted from an *ex-situ* sample prepared on a two-electrode silicon chip by constant current deposition from an electrolyte of 0.1 M $CuCl_2.2H_2O$ (reagent grade, ≥99%, Sigma-Aldrich) in milli-Q water (20 ppm) for 2 minutes (min), which resulted in finely segregated species of Cu(I) and Cu(0), and some amount of precipitated $CuCl_2$ salt on the window surface. Electrochemically, it was a failed experiment as the potential was not controlled during the deposition process, leading to extensive water splitting. However, analysis of the resulting electrodeposited materials provided a good source of reference NEXAFS spectra for cuprous species.

Copper metal reference samples were prepared on similar two-electrode silicon chips by electrodeposition. The chemicals used were, cupric sulphate pentahydrate ($CuSO_4.5H_2O$, reagent grade, Sigma-Aldrich, $\geq$98%) and sulphuric acid (H_2SO_4, reagent grade, Sigma-Aldrich, 95-98%). Cu(0) was electrodeposited at -0.5V for 20 seconds (s) from an electrolyte of 10 mM $CuSO_4$ in 0.1 M H_2SO_4 solution, on the Au electrodes of the two-electrode silicon chip.

3.3.2 Influence of pH on Cu electrochemistry: CV study

As a preliminary step, the cyclic voltammetric response of the system to the pH of electrolyte was measured in a classic 3-electrode system in a beaker, using pure Au wires as working and counter electrodes and a Ag/AgCl reference electrode. Electrolytes of different pH were prepared using H_2SO_4, $CuSO_4.5H_2O$ and sodium sulphate (Na_2SO_4, reagent grade, Sigma-Aldrich, $\geq$99%). The electrolyte pH was controlled using calculated dilutions of H_2SO_4. To minimize the IR drop during the CV experiments, the concentration of SO_4^{2-} ions was maintained at 0.1 M by using Na_2SO_4 as a supporting electrolyte. The systems studied had solution compositions of 10mM $CuSO_4$ + (0.1 – x) M Na_2SO_4 + x M H_2SO_4 (pH 1.0 – 4.5, at 0.5 unit increments). After immersing the three electrodes into the cell, 3 cycle CV scans were done in the potential range of -0.7 to 0.7 V at a sweep rate of 50 mV/s using the Ivium potentiostat which was described in **section 2.3**.

3.3.3 Preparation of ex-situ samples for STXM

The *ex-situ* samples were prepared on the two-electrode silicon chips, for the pH range of 2 – 3.5 at a pH increment of 0.5 unit (the criteria for pH range selection discussed below), under two conditions of electrolyte; (i) with only pH adjusted without supporting electrolyte, [10mM $CuSO_4$ + x M H_2SO_4 (pH 2.0 – 3.5, at 0.5 unit increments)] and (ii) at constant ionic strength (adjusted using a supporting electrolyte), [10 mM $CuSO_4$ + (0.1 – x) M Na_2SO_4 + x M H_2SO_4 (pH 3.0 – 3.5, at 0.5 unit increments)]. Electrodeposition was carried out at two constant potentials for 5 s; at ca. -0.2 V w.r.t Ag/AgCl electrode (the point where the system just overcomes the double layer barrier), and at ca. -0.5 V w.r.t Ag/AgCl electrode (a large reduction potential where reaction is mass transfer controlled). Following the electrodeposition, the samples were washed for 2 minutes in a continuous stream of milli-Q water and dried inside a closed box under a fume hood before transport to CLS or ALS for STXM measurements.

Typically, depositions were made using a 3-electrode setup, with Ag/AgCl as the reference electrode. All depositions at -0.2 V were made on the left electrode of the Si_3N_4 window in a two-electrode silicon chip during which the right electrodes were used as the auxiliary electrode (see **Figure 3.1**). All depositions at -0.5 V were made on the right electrode.

3.4 Results & Discussion

3.4.1 NEXAFS reference spectra of Cu species

Multi-energy image scans (also called stacks), (Jacobsen, Wirick et al. 2000) in the energy range of 920-980 eV (Cu 2p edge) were measured on an (25 μm x 8 μm) area of electrode. The stack images were aligned and converted from transmitted intensity to optical density (OD) using the incident flux (I_0) spectrum extracted from an off-electrode region of the window which did not have deposited material. Regions of samples with pure Cu(I) and Cu(II) absorption spectra were identified by spectral fitting with aXis2000 (Hitchcock 2016). **Figure 3.2** presents quantitative maps of Cu(I) and Cu(II) areas in the measured area and their respective fits with the final reference spectra. Similarly, a Cu 2p stack was measured on a different sample where the deposition generated mostly Cu(0). **Figure 3.3** presents maps of Cu(0) and Cu(I) derived by fitting that stack to Cu(0) and Cu(I) reference spectra. Regions of pure Cu(0) were identified from the spectral fitting. The Cu 2p spectra of Cu(0), Cu(I) and Cu(II) obtained from these two stacks are in good agreement with Cu 2p spectra reported in the literature: Cu(0) (Fink, Müller-Heinzerling et al. 1985, Pompa, Li et al. 1991), Cu(I) species (Hulbert, Bunker et al. 1984, Grioni, Goedkoop et al. 1989, Tjeng, Chen et al. 1992) and Cu(II) (Grioni, Goedkoop et al. 1989, Tjeng, Chen et al. 1992).
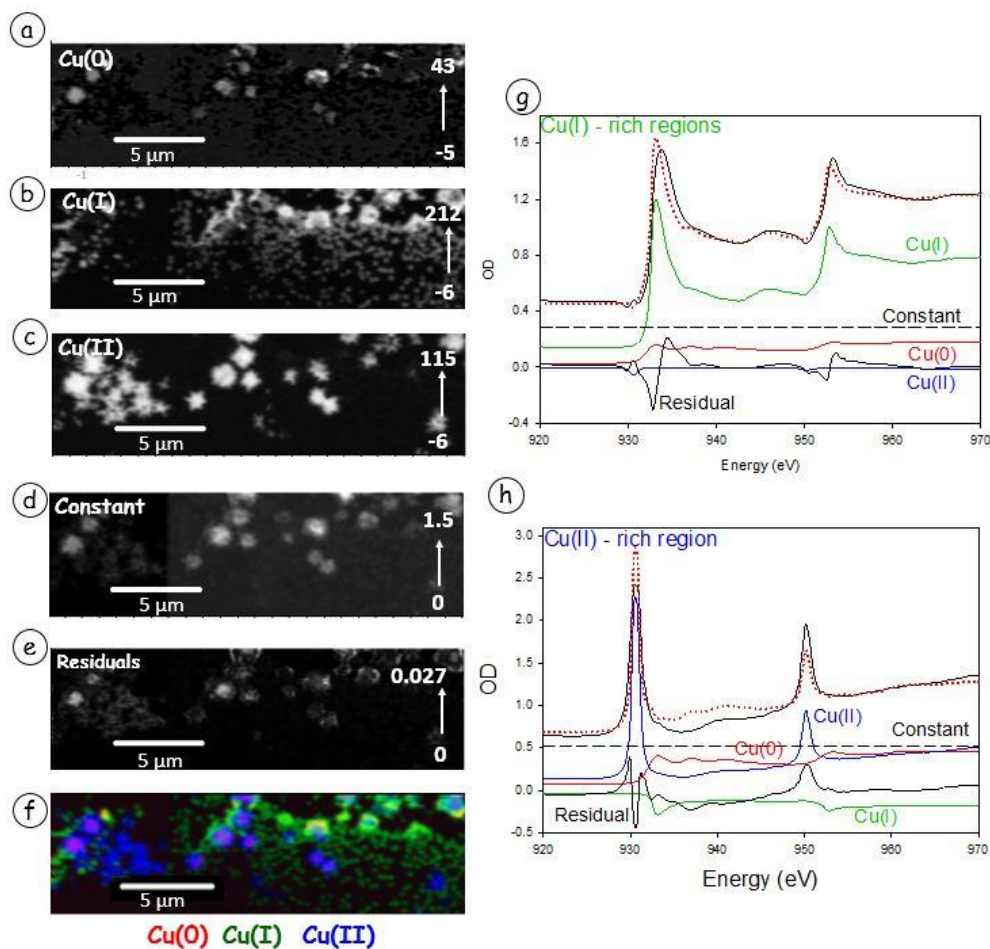
Figure 3.2 Results of a fit of the Cu 2p stack of the Cu(I) and Cu(II) species. (a) Cu(0) component map, (b) Cu(I) component map, (c) Cu(II) component map, (d) constant signal at all energies, (e) residual of the fit, averaged over all energies, (f) colour coded component map Red=Cu(0), Green=Cu(I), Blue=Cu(II), (g) spectral fit of the spectrum of Cu(I)-rich areas, (h) spectral fit of the spectrum of Cu(II)-rich areas**.**

37
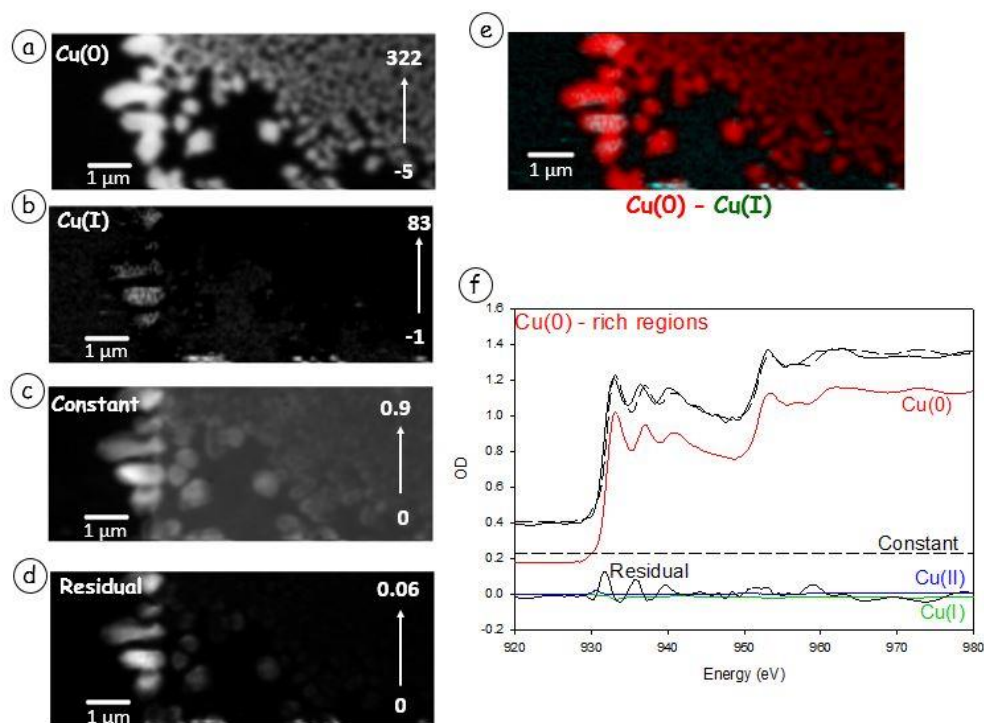
Figure 3.3 Fit of a Cu 2p stack of an electrodeposited copper metal sample to the reference spectra. (a) Cu(0) component map, (b) Cu(I) component map, (c) constant signal at all energies, (d) residual of the fit, averaged over all energies, (e) colour coded component map Red=Cu(0), and Green=Cu(I), and (f) fit of the spectrum of Cu(0) rich areas to the reference spectra.
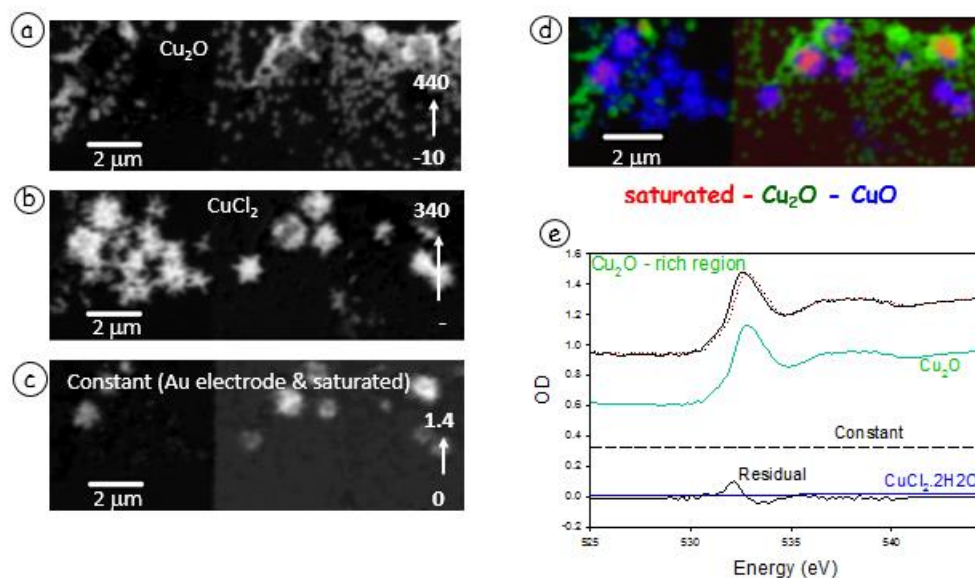
Figure 3.4 Results of analysis of O 1s stack from area for which the Cu 2p spectra are shown in Fig. 3.2. (a) Cu_2O component map, (b) $CuCl_2.2H_2O$ component map, (c) constant map (electrode), (d) colour coded component map Red=absorption saturated, Green=Cu(I), Blue=Cu(II), and (e) fit of the spectrum of Cu_2O-rich areas to the derived O 1s reference spectra.

Stacks of the same area where the Cu 2p spectra of Cu(I) and Cu(II) were obtained, were also measured at the O 1s edge (524-560 eV), aligned, and converted to chemical component maps (**Figure 3.4**). The O1s X-ray absorption spectra from Cu(I)-rich was found to be similar to O 1s spectra reported for cuprous oxide (Cu_2O) (Nakai, Mitsuishi et al. 1987, Grioni, Van Acker et al. 1992, Tröger, Yokoyama et al. 1994). Based on the spectral similarity the Cu(I)
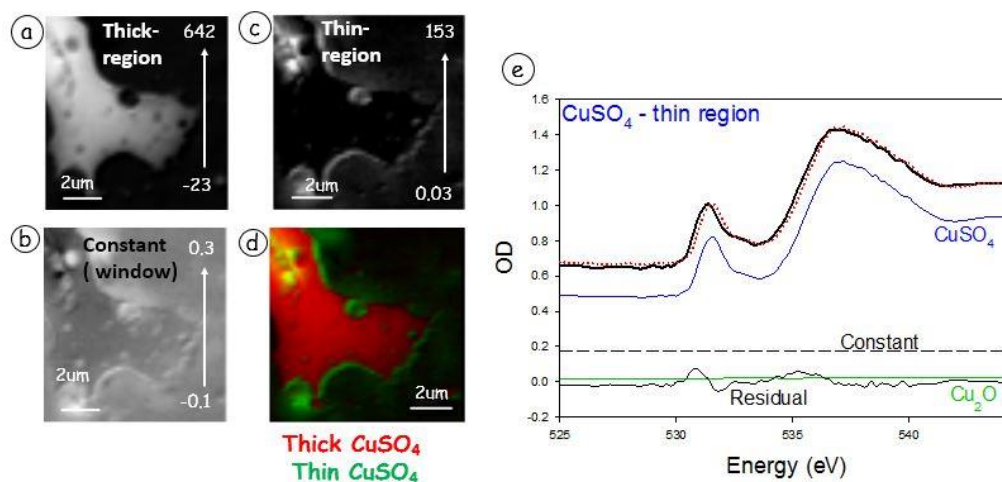
Figure 3.5 Results of analysis of O 1s stack of pure $CuSO_4.5H_2O$ sample (a) Thick area map, (b) Thin area map, (c) constant map (window), (d) Colour coded component map Red=Thick, and Green=Thin, and (e) Spectral Fit of spectra from $CuSO_4$-thin area to the derived O 1s reference spectra.

species deposited was attributed to Cu_2O. But, the Cu(II) species was precipitated from the original electrolyte solution ($CuCl_2.2H_2O$) and it could not be used as a O 1s reference spectrum in this study. This is because the electrolytes used in both *ex-situ* and *in-situ* studies were aqueous solutions of $CuSO_4$. So, an O 1s edge (524 – 560 eV) reference spectrum of $CuSO_4$ was measured from pure $CuSO_4.5H_2O$ compound dropcast on Si_3N_4 window (**Figure 3.5**). The O 1s reference spectrum extracted for $CuSO_4$ is in agreement with the literature O 1s spectrum of $CuSO_4$ (Chen 1997, Todd and Sherman 2003).

In order to obtain quantitative results from subsequent STXM measurements the Cu 2p and O 1s reference spectra were converted to an absolute OD1 scale - spectral response of 1 nm of the material at standard density (Hitchcock 2012). The as-measured spectra were scaled to match the pre- and post- edge signals to that in the X-ray absorption spectrum for the elemental formula (Henke, Gullikson et al. 1993), using standard densities of Cu_2O (6.0 g/cm^{-3}) (Madelung, Rössler et al. 1998), Cu metal (8.96 g/cm^{-3}) and $CuSO_4$ (2.28 g/cm^{-3}). **Figure 3.6** presents the Cu 2p OD1 spectrum of the Cu(II) species and the O 1s OD1 spectrum of the Cu(I) species (as Cu_2O) along with the elemental spectra to which the relative spectra were matched outside the near edge region to obtain absolute OD1 reference spectra. **Figure 3.7** presents the final Cu 2p and O 1s OD1 spectra Cu_2O, $CuSO_4.5H_2O$ and Cu metal.
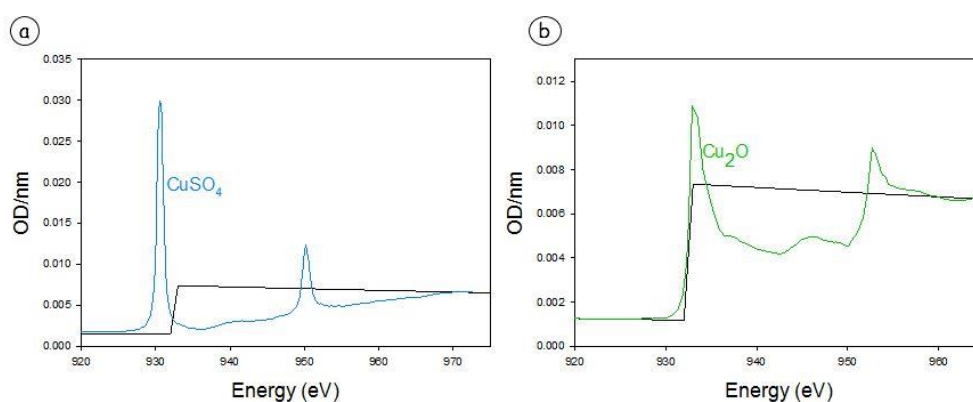
Figure 3.6 Cu 2p OD1 reference spectra of (a) Cu(II) and (b) Cu(I) species, matched to the calculated elemental response at pre- and post- edge.
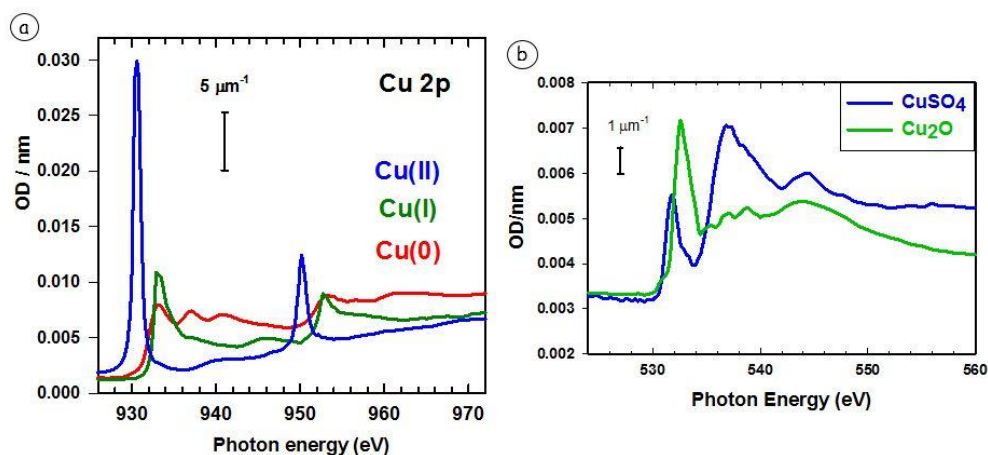
Figure 3.7 OD1 reference spectra of Cu species at (a) Cu 2p edge, (b) O 1s edge.

3.4.2 Cyclic voltammetry studies

Figure 3.8a & 3.8b presents cyclic voltammograms (CV) obtained for different pH solutions in the presence and absence of Na_2SO_4 as supporting electrolyte, measured under *ex-situ* conditions. These CV curves are consistent with the reported literature on Cu electrochemical systems (Danilov, Molodkina et al. 2005). The peak oxidation and reduction potentials shift closer to zero with increasing pH, an effect which was reproducible for up to 3 cycles at each pH. A shoulder was noted at the oxidation curves for the pH 2.5 and pH 3.0 electrolytes (**Figure 3.9**).
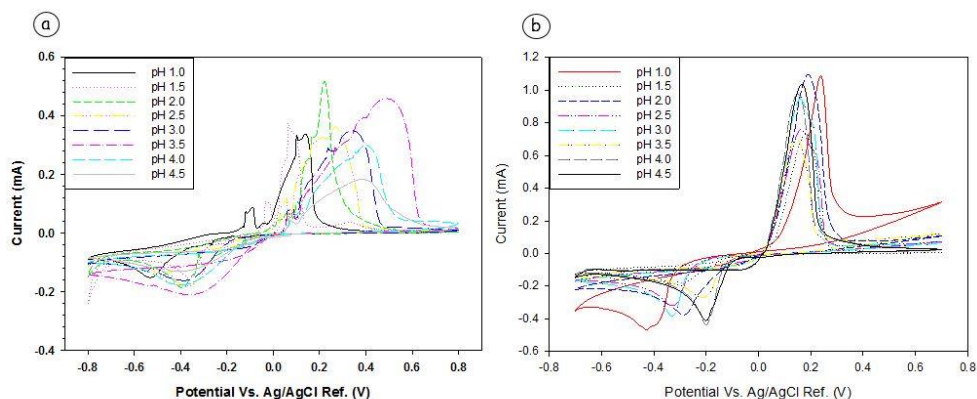
Figure 3.8 Cyclic voltammograms (CV) from solutions of (a) 10 mM CuSO$_4$
at pH 1.0 – 4.5 without added ionic species, scanned over -0.8 V to 0.8 V at 50
mV/s sweep rate. (b) CV from solutions at constant ionic strength [10 mM
CuSO4 + (0.1 – x) M Na$_2$SO$_4$ + x M H$_2$SO$_4$] at pH 1.0 – 4.5, scanned over -0.7
V to 0.7 V at 50 mV/s sweep rate.

The additional oxidation process was found to be reproducible over 3
cycles of scan, which suggests that an additional reduced species is produced
during the reduction scan, which is then subsequently oxidized (Bard and
Faulkner 2001). The main oxidation peak at ca. 0.2 V is from oxidation of Cu(0)
to Cu(II) (**eqn. 3.1**) because an analogous feature is found at all the other pH.

$$Cu^0 \text{ (s)} \rightarrow Cu^{2+} \text{ (aq)} + 2e^-$$ (**eqn 3.1**)

The second peak has a current intensity lower than that of the first peak, which suggests the possibility of a 1 electron transfer step resulting from oxidation of Cu(I) to Cu(II) (**eqn 3.2**).

$$Cu^{1+} (aq) \rightarrow Cu^{2+} (aq) + 2e^- \qquad\qquad \textbf{(eqn 3.2)}$$

Based on this, a broader pH range (pH 2.0 – 3.5), which included pH 2.5 and 3.0 where the additional features were observed, was selected for an *ex-situ* STXM study of the stabilization and the distribution of Cu(I) and Cu(0) species upon electrodeposition.

3.4.3 Cu electrodeposition: ex-situ studies

3.4.3.1 pH dependent electrodeposition – varying ionic strength

Cu 2p stacks were recorded from a 10 μm x 5 μm area on the *ex-situ*
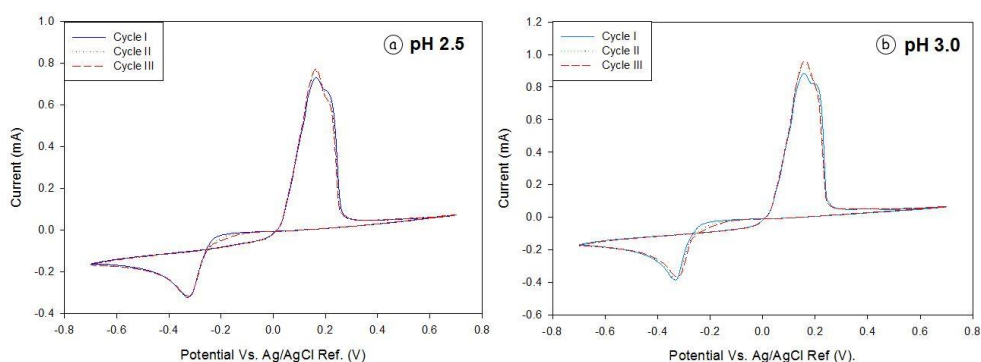
Figure 3.9 CV curves at (a) pH 2.5 and (b) 3.0 measured from constant ionic strength solutions

samples prepared on two electrode silicon chips. The transmission images were aligned, and converted to OD images using internal I_0 spectra. The Cu 2p OD stacks were fit with the Cu 2p OD1 reference spectra of Cu metal, Cu_2O and $CuSO_4.5H_2O$ to obtain component maps of each of the 3 species. **Figure 3.10** presents rescaled color-coded composites of the 3-component maps for each of the pH conditions studied.

The chemical composite maps show that a mix of Cu(I) and Cu(0) species was deposited at all pH. Visually, the samples at pH 3.0 and 3.5 show thicker deposition of Cu(I) species (more green), which indicates there is improved stabilization of Cu(I) at this intermediate pH range. Almost all the samples were found to have trace amounts of Cu(II) species, probably due to inadequate washing time leading to precipitation of electrolyte during drying of the samples.

Similarly, O 1s stacks were measured in the same areas, and aligned, converted to OD and fit to the O 1s OD1 reference spectra of Cu_2O and $CuSO_4$ using the stack fit procedure in aXis2000. **Figure 3.11** presents rescaled color composites of the components derived from the O 1s stack. The Cu(0) signal was estimated from the constant map of the fit, after subtracting the internal absorption signal from the electrode.
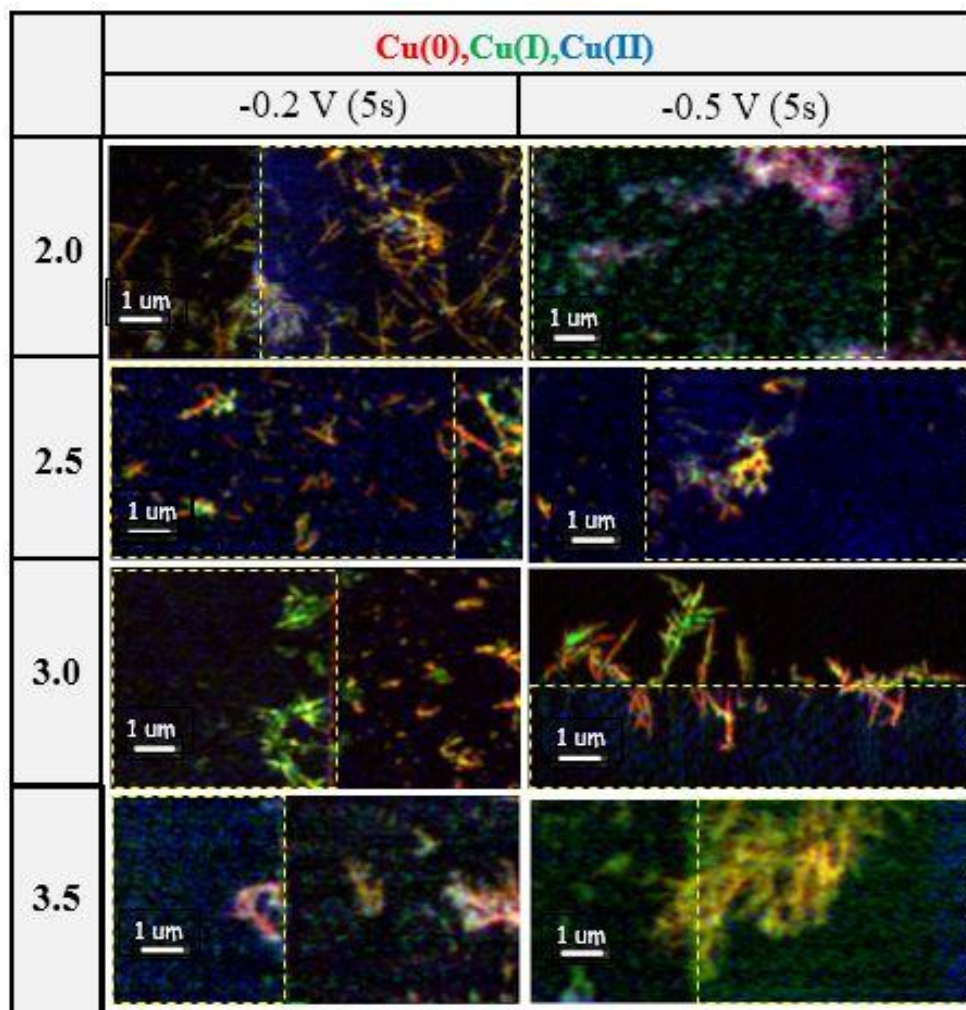
Figure 3.10 Spatial distributions of Cu(0), Cu(I) and Cu(II) species in *ex-situ* electrodeposited samples at indicated pH and deposition potential, derived from fits to Cu 2p stacks. Red = Cu(0), Green = Cu(I) and Blue = Cu(II). Dotted lines indicate electrode position.
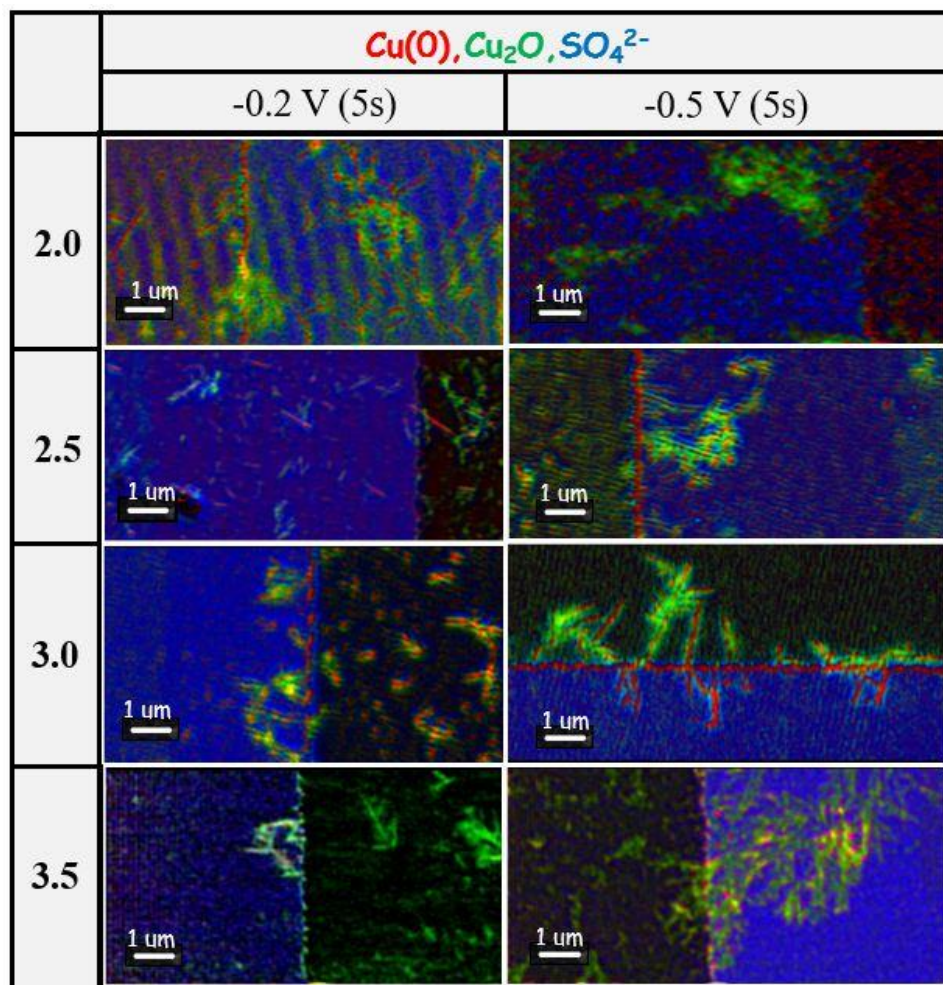
Figure 3.11 Spatial distributions of Cu(I) as Cu$_2$O, Cu(0) and electrode surface, SO$_4^{2-}$ derived from fits to O 1s stacks in same areas as Fig. 3.10. Red = Cu(0), Green = Cu(I) and Blue = Electrode (SO$_4^{2-}$).
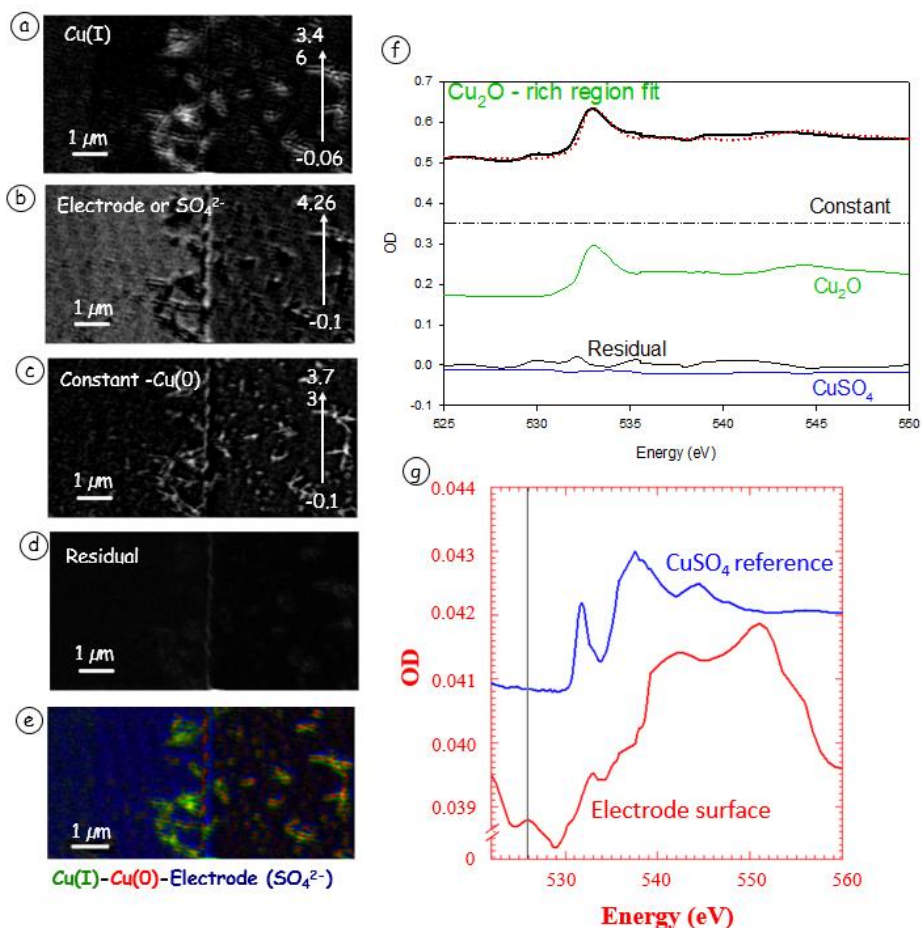
Figure 3.12 Results of fitting an O 1s stack of a sample electrodeposited at pH 3.0 and -0.2 V to the reference spectra showing Cu(I) rich areas; (a) Cu(I) component map, (b) electrode component map, (c) constant signal at all energies, (d) residual of the fit, averaged over all energies, (e) Colour coded component map Red=Cu(0), Green=Cu(I), and Blue=electrode, (f) spectral fit of Cu(I) rich areas, (g) plot comparing spectral features from the electrode surface to the $CuSO_4$ O1s edge reference spectra.

The O 1s spectra extracted from the Cu(I)-rich regions show that the Cu(I)

species deposited is Cu_2O (see **Figure 3.12f**). There is a strong Cu(II) absorption

signal all over the surface of the electrode which was initially thought to be

adsorbed SO_4^{2-} ions but these are not well represented by the O 1s reference

spectrum from $CuSO_4$ (see **Figure 3.12g**). There are no spectral evidence of the

adsorption of SO_4^{2-}, so there has to be a cationic species associated in this

(Wieckowski, Zelenay et al. 1991), which requires further S 2p edge studies on

deposited species. However, this work focusses on the distribution of

electrodeposited Cu(I) and Cu(0) species. Studies at S 2p edge is proposed as

directions for further research in this area (**chapter 6**).

3.4.3.2 Constant Ionic Strength Electrodeposition

A similar study on pH-dependent Cu electrodeposition was carried out

using added Na_2SO_4 electrolyte to establish constant ionic strength. In this case,

the peak oxidation and reduction currents are the same at all pH indicating the

electrolyte conductivity was constant (see **Figure 3.8b**). Cu 2p stacks were

measured, aligned, converted to OD and fit with the Cu 2p edge reference spectra

of Cu(I), Cu(0) and Cu(II) species. **Figure 3.13** presents the spatial distribution

maps of Cu(I), Cu(0) and Cu(II) species as a function of pH at constant ionic

strength of the electrolyte solution. In this case only Cu metal was observed.

There was no sign of Cu(I) at any pH. This indicates that a low IR drop (constant,

high ionic conductivity) at all pH overrides the stabilization of Cu(I) which was

expected to occur at intermediate pH range (pH 2.5 – 3.5).
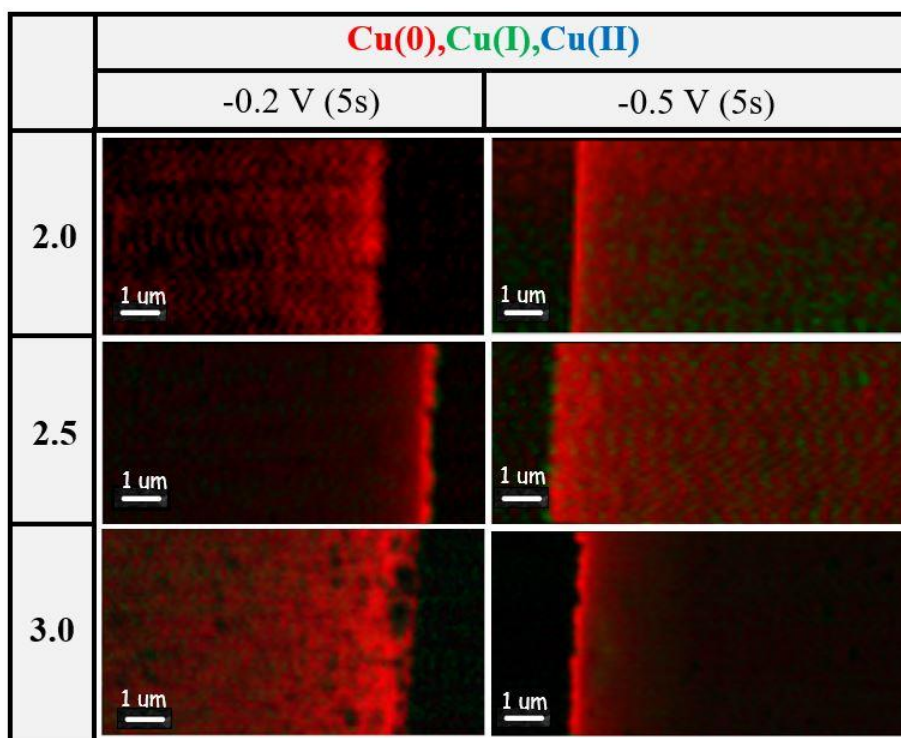
Figure 3.13 Spatial distributions of Cu(I), Cu(0) and Cu(II) electrodeposited at constant ionic strength, derived from fit to a Cu 2p stack. Red = Cu(0), Green = Cu(I) and Blue = Cu(II).

The electrochemical characterization of the pH dependence of Cu electrochemistry at constant ionic strength in a beaker showed the additional shoulder on the oxidation side, which was interpreted as a 1-electron Cu(I) →

Cu(II) oxidation (see **Figure 3.9**). But the *ex-situ* STXM studies suggests that the interpretation of the shoulder on the oxidation side of the CV may be wrong. Clearly, this is a situation where *in situ* studies with controlled applied potential might shed light on the mechanism involved.

3.4.3.3 Quantitative Analysis

Distributions of Cu(I) and Cu(0) were measured from samples prepared *ex-situ* under pH control with and without control of electrolyte conductivity. To identify a specific condition (pH, potential and ionic strength) which resulted in a higher fraction of Cu(I) with respect to Cu(0), quantitative analysis was performed. **Figure 3.14** is a flow diagram of the analysis method.

Since OD1 spectra were used to determine the spatial distribution of each of the Cu species, the intensity of each pixel in a component map is the thickness (in nm) of the component at that pixel. Regions with statistically significant levels of the material of interest are threshold masked (see **Figure 3.14)** to generate a region of interest (ROI). The ROI is applied to the OD stack to extract the average spectrum of that ROI. Alternatively, the component map is multiplied by the threshold mask which gives a map in which statistically significant levels of the material are present. The average value of non-zero pixels in the thresholded map is then generated which is the average thickness of the component in the area

measured. Based on the average thickness, standard density and area of deposited components, the mass of a component can be calculated by **eqns. 3.3 & 3.4**.

$$Density, \rho = \frac{Mass\ (m)}{Volume\ (V)} = \frac{Mass\ (m)}{[Thickness\ (t) \cdot Area\ (A)]}$$ **eqn. 3.3**

$$Mass, m = \rho \cdot t \cdot A$$ **eqn. 3.4**

Figure 3.15 presents quantitative results for Cu(I) and Cu(0) at different pH at potentials of -0.2 V and -0.5 V. The bar chart for Cu(I) deposition at -0.2 V and -0.5 V (**Figure 3.15a**) indicates that the highest amount of Cu(I) is deposited at pH 3.0 at a potential of -0.2 V.
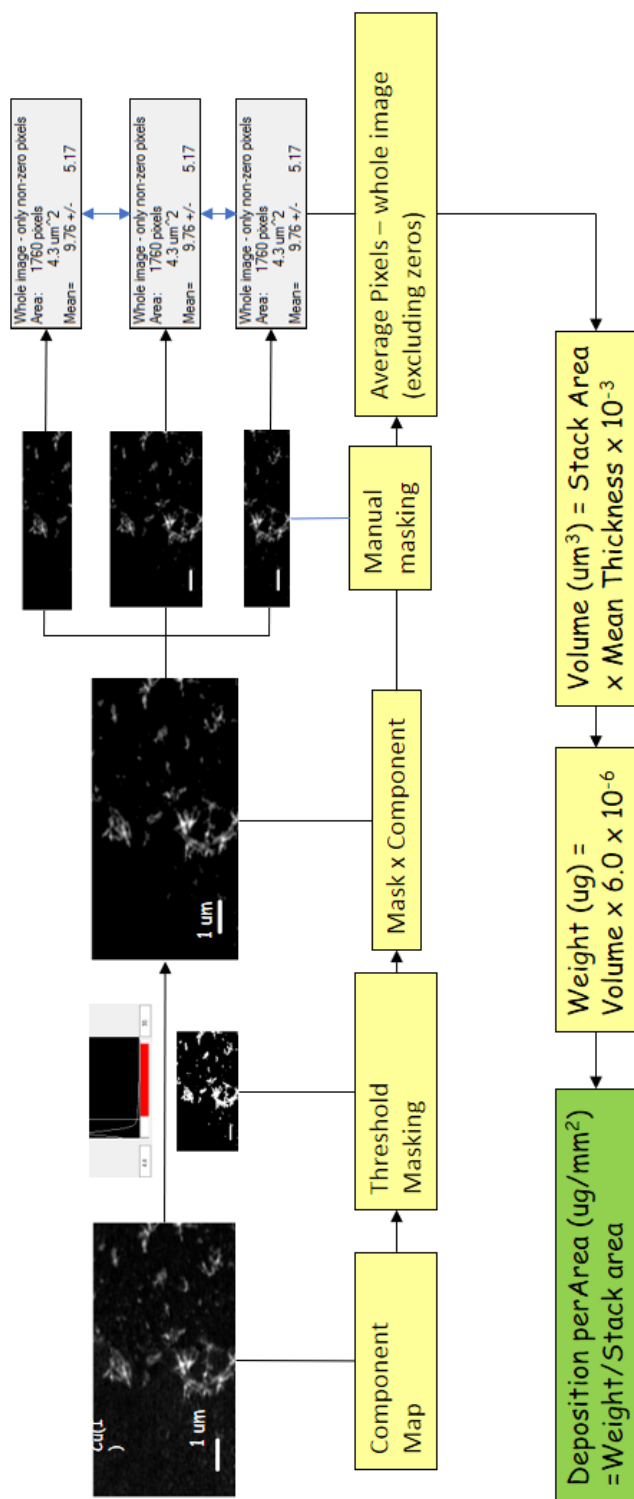
Figure 3.14 Flow scheme showing how the amount of Cu(I) in an *ex-situ* sample was determined.
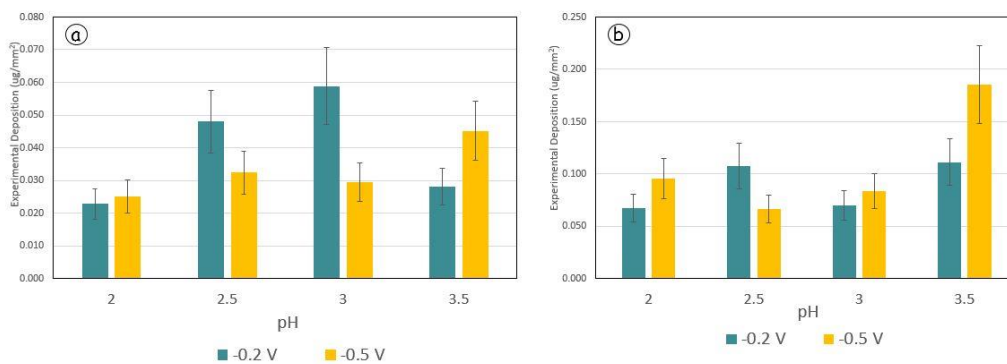
Figure 3.15 Bar charts of (a) amounts of Cu(I) obtained at various pH at -0.2
and -0.5 V, (b) amounts of Cu(0) obtained at various pH at -0.2 and -0.5 V.
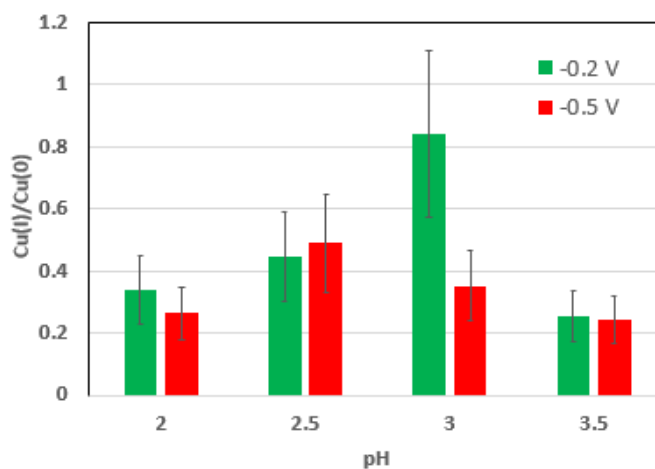
Figure 3.16 Bar charts of the ratio of Cu(I) to Cu(0) deposited at –0.2 V and -
0.5 V at different pH.

Figure 3.16 presents the ratio of Cu(I) to Cu(0) deposited at different pH at potentials of -0.2 V and -0.5 V. The bar chart at -0.2 V (**green**) and pH 3.0 indicates that the ratio of Cu(I) to Cu(0), is near 1 under these conditions, which indicates an improved stabilization of Cu(I) relative to other pH and potential conditions.

Combining the inferences from **figures 3.15** and **3.16**, Cu(I) stabilization in electrochemical deposition of copper from aqueous solutions is the highest when deposition is carried out at a potential of -0.2 V at pH 3.0 of aqueous $CuSO_4.5H_2O$ solution, without added supporting electrolyte.

3.5 Conclusions

Based on *ex-situ* studies conducted without control of ionic conductivity, Cu(I) species are stabilized at pH~3.0. However, there was no condition in aqueous acidic electrolyte which resulted in exclusive deposition of Cu(I). *Ex-situ* studies at constant ionic strength, providing ~10^2 times higher electrolyte conductivity, showed that pure Cu(I) cannot be deposited at any pH regime studied.

This observation can be explained by considering the concentration of OH^- ions present under the two conditions of electrolyte conductivity. Under both cases at all pH, driving the system/WE to an overpotential initiates adsorption of OH^- and SO_4^{2-} anions to the Au electrode surface, followed by nucleation of Cu

adatoms at the adsorption sites (Danilov, Molodkina et al. 2005, Wu, Yin et al. 2011). The rate of adsorption is influenced by the anionic concentration and the pH of the electrolyte. In general, electro-adsorption of SO_4^{2-} ions is lower in weakly acidic solutions (Wieckowski, Zelenay et al. 1991).

In the studies without control of ionic conductivity, the only source of SO_4^{2-} ions is from dissociation of $CuSO_4$ in water. At intermediate pH (weak acidity), a reduced rate of SO_4^{2-} adsorption leads to more OH^- adsorption sites for nucleation of Cu adatoms (Danilov, Molodkina et al. 2005). Since, Cu(I) is readily stabilized with OH^- ions on the surface of electrode, the conditions with greater surface $[OH^-]$ lead to an intermediary chemical step to form Cu_2O species, as was observed in STXM studies in the electrolytes of pH range of 2.3 - 3.5 without control over electrolyte conductivity. In strongly acidic conditions, the presence of adsorbed SO_4^{2-} prevents OH^- adsorption and thus any Cu(I) produced electrochemically is not stabilized, but rather further reduces to Cu metal. Based on these considerations, the following mechanism is proposed:

In *strongly* acidic electrolyte, an **EE** (Two consecutive electrochemical steps) mechanism is followed:

    i.   *SO_4^{2-} adsorption: SO_4^{2-} + Au $\rightarrow$ (Au- - SO_4^{2-})$_{ads}$ + H^+ (<u>fast</u>)*

    ii.   *OH^- adsorption: OH^- + Au $\rightarrow$ (Au- -OH^-)$_{ads}$ + H^+*

    iii.   *Nucleation: Cu^{2+} + e^- $\rightarrow$ Cu^{1+} [Electrochemical step (**E**)]*

                                   *Cu^{1+} + e^- $\rightarrow$ Cu^0 [**Electrochemical step (E)**]*

    iv.   *Growth of deposits.*

In *weakly* acidic electrolyte, an **ECE** (two electrochemical steps with an intermediary chemical step) mechanism is followed:

    i.   *SO_4^{2-} adsorption: SO_4^{2-} + Au $\rightarrow$ (Au- - SO_4^{2-})$_{ads}$ + H^+ (<u>slow</u>)*

    ii.   *OH^- adsorption: OH^- + Au $\rightarrow$ (Au- -OH^-)$_{ads}$ + H^+*

    iii.   *Nucleation: $2Cu^{2+}$ + $2e^-$ $\rightarrow$ $2Cu^{1+}$ [**Electrochemical step (E)**]*

                                   *Cu^{1+} + OH^- $\rightarrow$ Cu_2O + H^+ [**Chemical Step (C)**]*

                                 *Cu^{1+} + e^- $\rightarrow$ Cu^0 [**Electrochemical step (E)**]*

    iv.   *Growth of deposits.*

    More details on various types of mechanisms of electrochemical reactions can be found elsewhere (Bard and Faulkner 2001).

In studies conducted at constant ionic strength of the electrolyte, the SO_4^{2-} ions are always in excess through all pH. A high concentration gradient of SO_4^{2-} shifts the adsorption equilibrium even in a weakly acidic electrolyte. This reduces the rate of OH^- adsorption and results in deposition of pure Cu metal. This mechanistic discussion suggests that a high $[SO_4^{2-}]$ in the electrolyte plays a major role in obtaining pure Cu(0) deposits without any impurities of Cu(I), irrespective of the pH. Alternatively, the changed distributions could be solely related to improving the ionic conductivity of the solutions. These two explanations could be differentiated by repeating the measurements at constant ionic strength, but without using Na_2SO_4 as the supporting electrolyte. Alternate ionic salts such as sodium acetate or potassium iodide, KI could be used. This opens scope for further investigations on determining if it is the high $[SO_4^{2-}]$ or just high ionic conductivity of the electrolyte that influences Cu(I) stabilization. These possible future experiments are discussed in detail in **chapter 6**.

CHAPTER 4.   DESIGN AND DEVELOPMENT OF *IN-SITU*

ELECTROCHEMICAL FLOW CELL

This chapter describes the design of the in-situ electrochemical flow cell used in this research. It discusses the spatial constraints imposed by STXM on the holder design, and summarizes various stages of holder design which have evolved to the existing Phase 1b Holder. The chapter concludes with a step-by-step guide to assembly of a flow cell.

4.1 Introduction

In-situ electrochemical STXM without electrolyte flow was previously demonstrated by our group using two different designs of silicon chip devices (Guay, Stewart-Ornstein et al. 2005, Hitchcock, Qin et al. 2016), which was marked as the phase 1 of this project. However, the goal of a reliable and reproducible *in-situ* <u>flow</u> electrochemical STXM required development of a new set of devices with advanced features and provision of flowing electrolyte. This stage of the project is referred to as phase 1b and the corresponding devices are called phase 1b devices. They consist of an electrode chip, a spacer chip, and a holder. The design and operation the holder is discussed in section 4.2. First, I present the design of the silicon wafer chips which form an electrochemical micro flow cell which was developed in collaboration with Norcada Inc (Norcada).

4.1.1 Design of electrode chip ('E')

Two custom silicon chips were fabricated, one with electrodes (chip 'E'),

the other with a channel defined by a spacer layer (chip 'F'). **Figure 4.1a** is a

CAD model of the phase 1b electrode chip. Two designs of electrode chip were

fabricated, namely E-I and E-II. Both the electrode chips 'E-I' and 'E-II' are 12

mm x 5 mm in size, 200 μm thick, and is equipped with 3 gold electrodes. The

electrodes are at a mm scale and 100 nm thick on most of the chip. They terminate

at μm scale electrodes, 25 nm thick, on the Norcada proprietary X-ray transparent

silicon nitride (Si_3N_4) membrane window which is 200 μm x 80 μm in size, and

100 nm thick.

The entire surface of the chips E-I and E-II, except the window and small

areas around the window (270 μm x 150 μm) and the electrical contact pad of the

electrodes (5 mm x 2.5 mm) at the top, is coated with a hydrophilic, electrically

insulating SiN_x layer to ensure that almost all of the observed electrical signal

comes from the window area where STXM studies can be performed. Two square

inlet and outlet ports (0.8 mm x 0.8 mm), placed with vertical offsets, are etched

through electrode chip 'E' to allow provision for flow of liquid electrolyte.
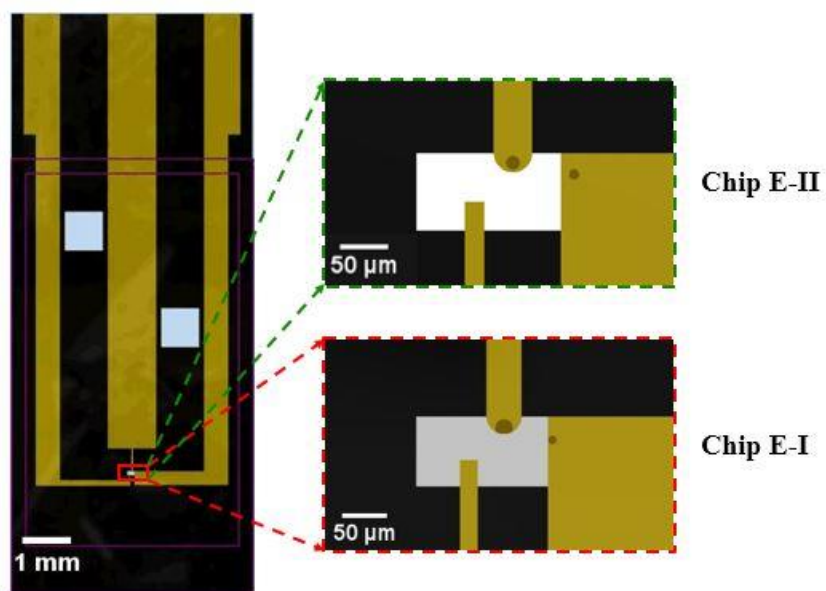
Figure 4.1 (a) CAD model of the phase 1b electrode chip **(b)** expanded view of the chip E-I and Chip E-II window area.

Figure 4.1b presents an expanded view of the window region, showing the design of the three electrodes in the window region. The center electrode with the hemispherical termination is used as the working electrode (W). The large electrode to the right is used as the counter electrode (C). The third, narrow electrode coming up from the bottom is used as the reference electrode (R). Together they form a three-electrode electrochemical cell system (Bard and Faulkner 2001).

The working and the counter electrodes each have circular thin areas, where the Au electrode is 20 nm thick. These thin areas were included in chip E

design to allow studies at the C 1s edge; the 100 nm Au thickness saturates the X-ray absorption below 500 eV. The E-I chips has this thin Au area on the edge of the electrodes while the E-II chips have this thin Au area moved inside the electrode area. This was done to have allow studies of electrochemical events at the electrode edge, where the electric field density and thus the electrochemical activity is higher.

The overall phase 1b electrode layout differs from other designs, which typically have the counter electrode surrounding the working electrode (Bozzini, Amati et al. 2013, Lim, Li et al. 2016). The phase1b electrode system has been designed differently, to be spacious and thus eventually able to accommodate deposition of porous carbon electrodes as the working electrode (see **section 6.2.1**). Another reason for the choice of the current electrode structure is to
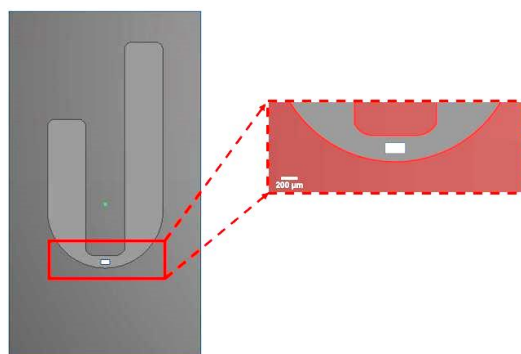
Figure 4.2 (a) CAD model of Phase 1b Spacer Chip **(b)** expanded view of the window region with flow channel.

minimize the chance of shorting of counter and working electrodes by electrodeposited dendrites, thereby enabling multiple cycles of deposition and stripping.

4.1.2 Design of spacer chip ('F')

Figure 4.2a represents a CAD model of the phase 1b spacer chip 'F'. It is 9 mm x 5 mm in size, 200 μm thick, and has a 240 μm x 120 μm, 50 nm thick X-ray transparent Si_3N_4 window. Most of the surface of chip 'F' is coated with a 1.5 μm thick insulating SiO_x hydrophobic spacer layer, leaving a 'J' shaped flow channel. The top ends of the 'J' channel align with the two diagonal flow ports on the electrode chip and arcs at the window of the spacer chip (**Figure 4.2b**). This 'J' channel defines the path of flow of the liquid electrolyte through the window region. The channel is deposited with a layer of hydrophilic SiN_x to facilitate flow of aqueous electrolyte within the channel. The idea is to enclose a 1.5 μm thick film of liquid electrolyte between the electrode and spacer chips. After assembly
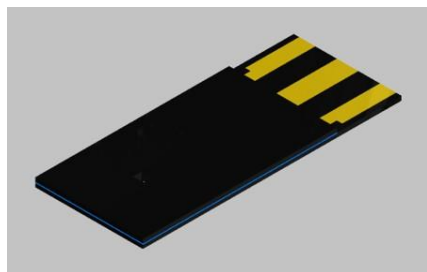
Figure 4.3 An assembled electrode-spacer chip pair.

and sealing the sandwich of the electrode chip as the downstream chip and the

spacer chip as the upstream chip a micro flow cell is formed, **Figure 4.3**.

4.2 Rapid prototyping of holders

4.2.1 Parameters influencing the design of holders

To mount the phase 1b system in STXM, to accommodate the chips, and

to set up the flow of electrolyte through the cell, required a trapezoidal holder that

fits into the 3-pin kinematic mount of STXM (Kilcoyne, Tyliszczak et al. 2003).

Before discussing the technical aspects of the holder, the spatial constraints of

STXM need to be considered. **Figure 4.4** is a schematic of the ambient-STXM (a-

STXM) at 10ID1 beamline at CLS. The major parameters to be considered while

designing a flow cell holder for STXM are:

- Soft X-ray transparency of the sample (1 – 1.5 μm electrolyte film).

- Positioning and operation of the electrochemical cell at the microscope
  focal point without collisions with the microscope components, in
  particular the OSA and the detector.

- Provision to introduce and remove electrolyte from outside STXM.

- Avoiding or accommodating evolution of gases (e.g. from water splitting
  in an aqueous electrolyte) during an *in-situ* electrochemical experiment.

- Leak-free system at high vacuum.
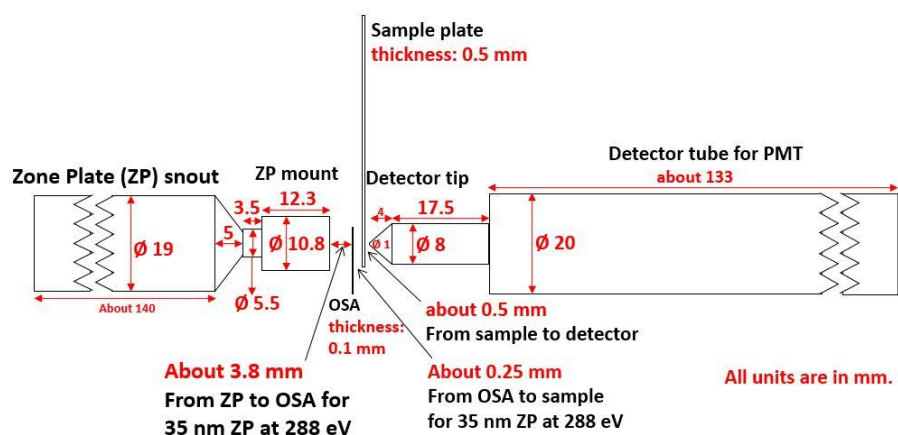
Figure 4.5 Schematic of ambient-STXM at 10ID1 beamline at CLS.
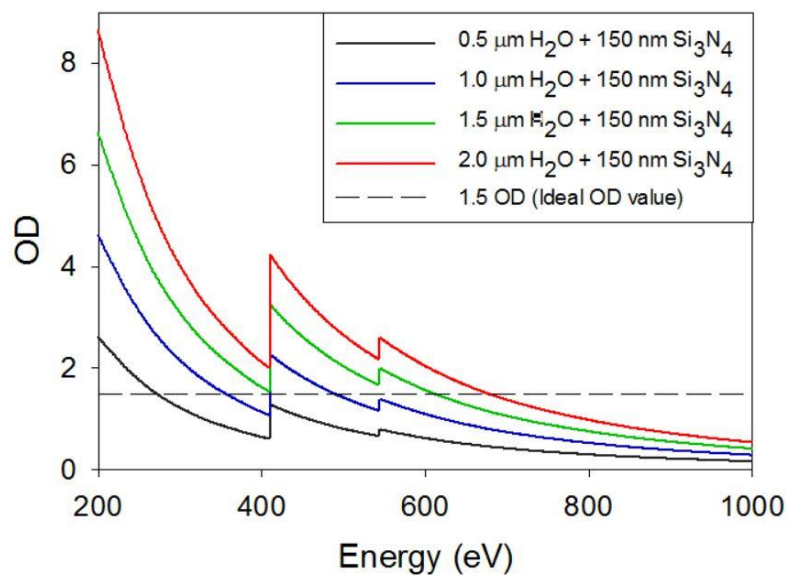
Figure 4.4 Calculated X-ray absorption OD plots for various thickness of fluid

film enclosed between 150 nm Si_3N_4 membrane.

The maximum optical density (OD) of a sample in STXM should be <2.5 for reliable spectral information without absorption saturation. For measurements below the O 1s onset (<532 eV) the thickness of an aqueous system with <2.5 OD is 0.5 – 1.0 μm and at energies far above (>700 eV) the thickness of an aqueous system with <2.5 OD is 0.5 – 2.0 μm (**Figure 4.5**), which is determined based on the relationship between transmitted X-ray intensity, optical density and thickness of the sample (eqn. **2.5**).

To perform STXM spectro-microscopy, it is essential that the sample is in focus. The focal length of a zone plate (ZP) varies linearly with the X-ray energy (**eqn. 2.8**). For measurements at the C 1s edge (285 eV) the focal length of a 240 μm diameter, 25 nm outer zone ZP is 1394 μm. For a 50 μm diameter OSA, the minimum sample – OSA distance is ~250 μm (**Figure 2.2**). Thus, it is possible to use 200 μm thick silicon for the upstream chip. However, due to the need to provide a system to compress the two silicon chips involved in the case of an *in-situ* flow cell in order to seal them, the thickness of the device upstream from the focal point will be significantly greater than 200 μm. Similarly, the active area of the detector is ~600 μm. At the C 1s edge the diverging transmitted light exceeds 600 μm when the detector is ~3.5 mm downstream of the sample (**see figure 2.4),** which is another limit on the thickness of the system downstream of the focal

point. These physical constraints must be accommodated in the design of the phase 1b holder.

Next, during operation of an electrochemical cell there could be instances of gas evolution due to events such as water splitting when the cell is driven to a high over-potential during *in-situ* experiments. The evolved gas can generate a high internal vapour pressure which can lead to fracture of the Si_3N_4 membrane and subsequent leakage of the electrolyte into the STXM chamber. One function of the continuous flow system is to remove these evolved gases.

Since soft X-rays are readily absorbed by air, the STXM chamber should be either high vacuum or have the air replaced with He, which is X-ray transparent. If vacuum operation is required, the *in-situ* flow electrochemical system inside the chamber needs to be 100% leak free. Even if the air is replaced by He (as was the case in the successful experiments performed in this thesis), it is important that any leak of electrolyte from the cell or fluid connections be minimal. Ideally, a design fully compatible with high vacuum is preferred for the *in-situ* flow electrochemical STXM.

4.2.2 Evolution of the phase 1b in-situ flow electrochemical STXM holder

Figure 4.6a presents a CAD model of the first version of the flow cell holder, which was fabricated by the McMaster machine shop according to the design by a graduate student (Zhisheng Qin) who worked on phase 1 of this

project. The holder was made from Delrin with angular flow vias from behind reaching the flow ports on the electrode chip ('A' - Phase 1). It marked the first successful demonstration of static copper electrodeposition and stripping (Hitchcock, Qin et al. 2016).

The electrode ('A') and spacer chips ('D') were assembled and sealed with 5-minute epoxy. Attempts to establish electrolyte flow were made using a machined flow adaptor designed to direct the electrolyte into the sandwich of chips (green structure in **Figure 4.6b**). But, *in-situ* flow electrochemistry with this device was never achieved since the electrolyte fluid layer was always too thick (X-ray absorption saturation). However, this was a major motivation to improve the system in the phase 1b design.
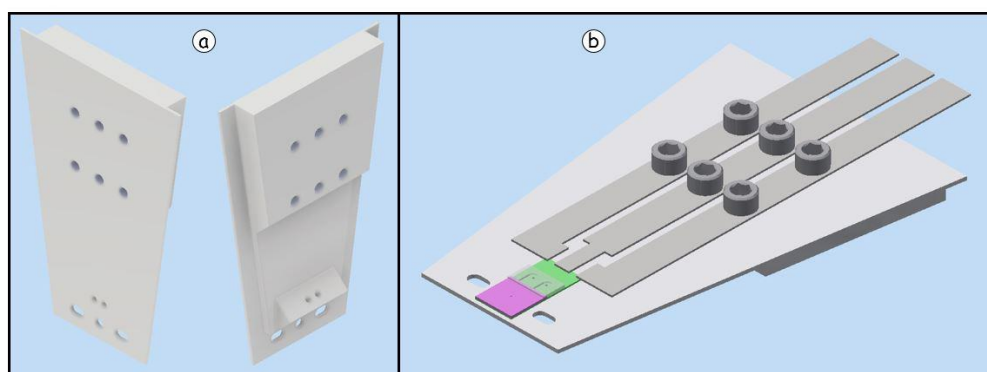
Figure 4.6 CAD model of phase 1 *in-situ* flow cell holder (a) holder, (b) assembled phase 1 device on holder.

4.2.3 Multi-jet Printing of Holders

During development of phase 1b devices, high resolution 3D printing was found to be a promising approach since it allowed cost-effective exploration of prototypes with advanced features with intricate designs. This lead to a series of 9 versions of the *in-situ* flow cell holder for the phase 1b chips. A Projet® 3510 HD *Plus* multijet 3D printer (3DSystems) was used for fabricating prototypes of holders. It uses UV-curable plastic (under the product range of Visijet® materials) and wax as the support material (Visijet S300). It has a maximum build envelope capacity of (298x185x203) mm and a layer resolution of 16 μm in the Xtreme High Defenition (XHD) mode (3DSystems). Among the available range of visijet materials, Visijet M3 Crystal (EX200) was selected to be compatible for our applications based on its physical and chemical properties (Visijet).

Once printed, the prototype is generally filled with wax (Visijet S300) as the support material. The part is then placed in a stream of water vapor for 15 minutes, which melts the wax support material. The remnants of support material in the small voids are removed by sonication in vegetable oil at ~50^0 C for 30 minutes. **Tables 4.1** and **4.2** summarizes the intermediate designs of holder that were examined for compatibility with the Phase 1b chips and the reasons for their failure. These intermediate efforts lead to the final design which is discussed in detail in the next section.

Table 4.1 An overview of the intermediary designs (1 - 5) of holder leading to

the present Phase 1b holder.
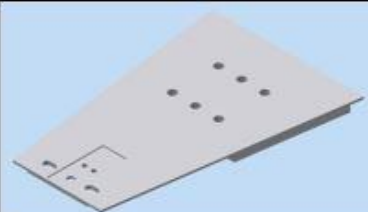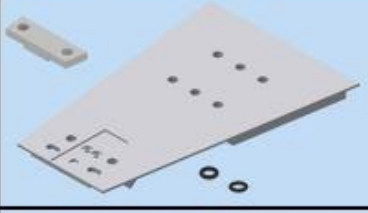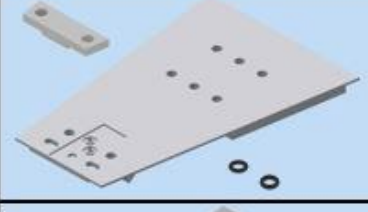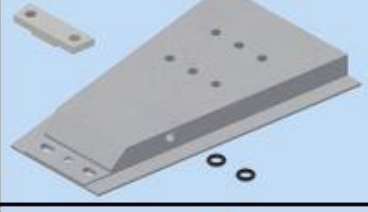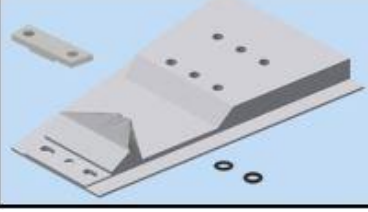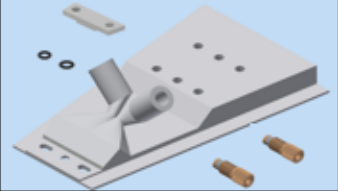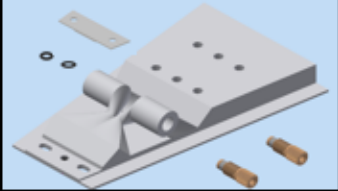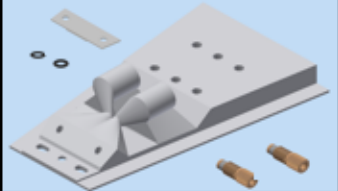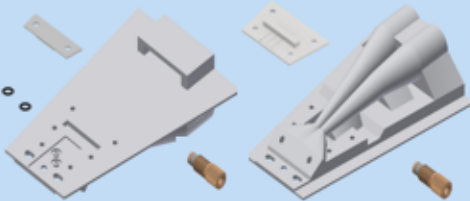
	Designs	Improvements	Reasons to Failure
1		- Provides more freedom to sample stage, as chips are embedded into the slot on holder.	- No proper flow system. - Leaks at the flow port. - Leaks on the edge of chips
2		- Ensures better seal at flow port and the edges. (non-vacuum conditions) - Keeper piece arrives.	- No proper flow system.
3		- Diagonal flow ports. - Larger o-rings, better seal.	- No proper flow system
4		- Front side reached near-final design. - First attempt for a better flow system.	- Flow system fails, as there were no available microfluidic fittings of the size.
5		- Flow system to use capillary tubes.	- Flow system fails due to leak at the junction of tubing and the flow port

Table 4.2 An overview of the intermediary designs (6 - 9) of holder leading to

the present Phase 1b holder.

	Designs	Improvements	Reasons to Failure
6		- First Flow system for a standard available microfluidic fitting. - Microfluidic fittings arrive.	- Unable to achieve continuous flow as the inner diameter in middle the flow system was too small.
7		- Horizontal flow system. - Wider duct inside the flow system.	- Flow system not durable, used to break upon tightening the fittings.
8		- Vertical flow system with durable support for the structure.	- Flow channel interferes with the light shield on detector.
9		- Effective biasing arrives, issues with flow channel solved, with better support and wider inner diameter of channel.	- All good but, could not be used under vacuum without epoxy. - Being used for *in-situ* studies with He filled into STXM chamber.
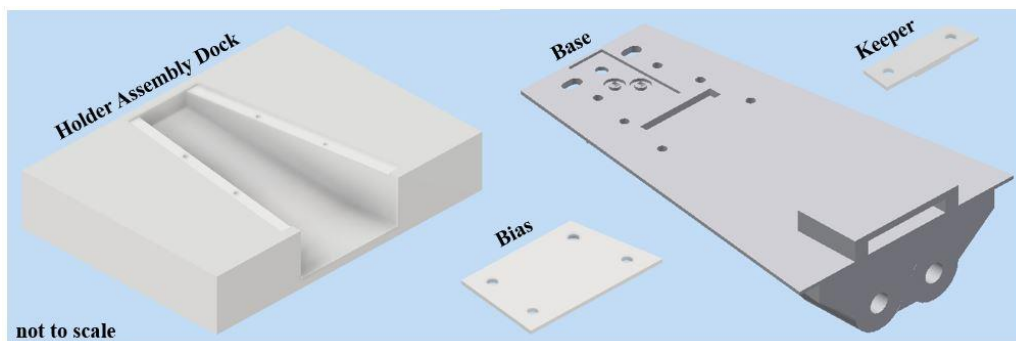
Figure 4.7 CAD models of 4 components of the phase 1b holder.

4.2.4 The Phase 1b in-situ flow electrochemical STXM Holder

The phase 1b flow cell holder has four components; the base, the keeper, the bias, and the holder assembly dock. These parts are assembled together with the phase 1b electrode and spacer chips using 00-80 NCF screws. **Figure 4.7** presents CAD models of the 4 components of the holder.

The base is designed such that it can house 1.5 mm(id.) x 4 mm (w) O-rings around the inlet and outlet channels, which aligns and plugs into the flow ports on the electrode chip upon assembly. It has two oval shaped holes on adjacent sides of the electrode chip housing, which can be used during experiments to measure the incident flux of X-rays (I_0). It has six 00-80 NCF sized tapped holes and a 1.5 mm wide rectangular slot, which is used to mount the keeper and the bias pieces.

The keeper is designed to mount over the electrode-spacer chip assembly, and is attached using two 00-80 NCF screws. Gently tightening the keeper piece compresses the O-rings establishing a fluid seal and holding the electrode-spacer chip assembly in place. More details of the cell assembly are presented in **section 4.3**.

The bias is used to establish electrical biasing between the potentiostat and the three electrodes on the electrode chip. The bias fits into the rectangular slot and ensures proper alignment of the electrical probe terminal with the electrode contact pads on the electrode chip.

The holder assembly dock is a platform on which an *in-situ* electrochemical flow cell is assembled. It has provision to mount the base unit on it and subsequent assembly of the other components of the holder.

4.3 Assembly of the phase 1b *in-situ* electrochemical flow cell device

4.3.1 Source and Specifications of components used

The *in-situ* electrochemical flow cell consists of; (i) the phase 1b electrochemical chips designed by me in collaboration with Dr. Hitchcock (McMaster University), Dr. Obst (University of Bayreuth), Dr. Harmer (Flinders university) and Mr. Hosseinkhannazer (Norcada Inc.) and fabricated by Norcada, (ii) the phase 1b holder, which I designed and had fabricated by 3D printing, and (iii) some

Table 4.3 List of components, specifications, and their source

S.no.	Component	Units	Specifications	Source
1	O-rings	2	1.5 (i.d)x0.45(h)	Somal Watch Parts, Canada
2	Epoxy	1	5-minute Epoxy	Bindulin, Germany
3	Microfluidic Fittings	2	M-660, M-650, P-349, PEEK	Idex Health & Science, USA
4	Female Leur to ¼-28 Female	2	P-628, PEEK	Idex Health & Science, USA
5	Connector Pins	3	Copper connector strip	University of Bayreuth, Germany
6	Tubing	2	ETFE, 1/8 inch (o.d)	Idex Health & Science, USA
7	Screws	6	00-80 NCF	M.Takeda Tools, Canada
8	Syringe Pump	1	NE-1010	New Era Syringe Pump, USA

commercially available parts/components. **Table 4.3** is a list of components and their respective specifications and source.

4.3.2 In-situ electrochemical flow cell assembly procedure

The following is a systematic guide to assemble a Phase 1b *in-situ* electrochemical flow cell. For convenience, the electrode chip will be referred to as chip E and the spacer chip as chip F.

1. Take a clean base of the holder and attach the inlet & outlet lines using microfluidic fittings (M-660 and M-650) and the ETFE tubing. Pre-fill the entire volume of inlet & outlet channels with electrolyte to completely minimize the dead volume in the system.

2. Place the O-rings into the grooves on the base. These will sit above the surface level of the holder, which is intentional, as it allows compressing the o-rings with the keeper piece to form a fluid seal. (**Figure 4.8**).
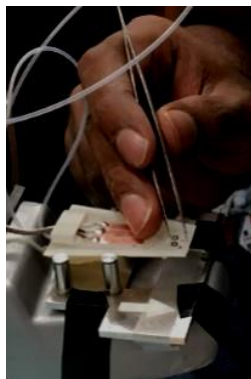
Figure 4.8 Placing O-rings into the groove.

3. Place the electrode chip into the rectangular housing for the chips, and
    ensure that the flow channel on the base plugs into the flow ports on the
    electrode chip. (**Figure 4.9**)
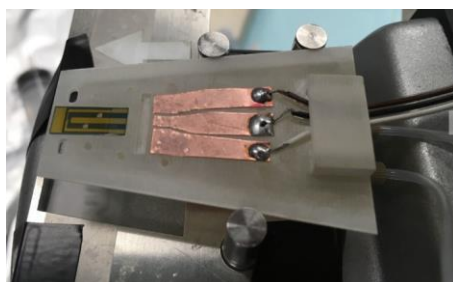
Figure 4.9 Placing the electrode chip (Chip E).

4. Use the bias piece to establish electrical connections on the electrode chip.
    Pre-insert four 00-80 screws and then fit the bias piece onto the base with
    the help of a tweezer and a fine tip screw driver. (**Figure 4.10**)

75

5. Ensure that the screws are tightened uniformly. Any uneven pressure on the bias piece may lead to cracking of chip E. The piece should be attached just tight enough to ensure electrical contact with the electrode contact pads on the chip E. Use a multimeter to ensure proper electrical connections.
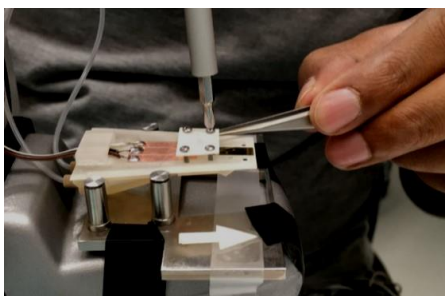
Figure 4.10 Assembling the bias piece.

6. Place chip F on chip E such that it aligns with the edges of chip E. Pre-insert the screws into their spots on the keeper piece. Fit the keeper on the base of the holder, and **gently** tighten the screws to apply enough pressure to compress the soft O-rings underneath, but not so much as to crack the window on either chip (**Figure 4.11**).

7. Seal the edges of the chip E-F junction using 5-minute epoxy. Allow it to

    cure for ~5 minutes. The flow cell is now ready to mount into STXM.

Figure 4.11 A completely assembled flow cell, ready to mount.

4.3.3 Determining flow rate of electrolyte

In a microfluidic device designed to perform *in-situ* electrochemical
studies it is desirable to have a laminar flow such that the reactants are actively
replenished without inducing any turbulence in the cell. In this work, a syringe
pump has been used to establish a stable and continuous flow of electrolyte
through the micro cell. The optimal flow rate was determined through Hagen-
Poiseuille calculations for the cross-section of the flow channel (in this case it is
rectangular), which can be done with an accuracy of 13% (Bruus 2015):

$$Q = \left[1 - 0.630\frac{h}{w}\right]\frac{h^3 w}{12\eta L}\Delta p \qquad \textbf{(eqn. 4.1)}$$

where, Q is the flow rate of electrolyte, h is the height of the spacer layer (1.5 μm), w is the width of the channel (1000 μm), η is the viscosity of electrolyte, L is the length of the channel (~10mm) and Δp is the pressure head between the inlet and the outlet flow ports on the chip assembly.

The pressure head, Δp can be calculated based on the desired average velocity of electrolyte through the window (V), using the Darcy-Weisbach formula with a Darcy friction factor (f) (White 2008):

$$\Delta p = f \cdot \left(\frac{L}{D_e}\right) \cdot \left(\frac{v^2}{2g}\right) \qquad \text{(eqn. 4.2)}$$

where, D_e is the equivalent diameter of the rectangular channel (diameter of a circular duct/pipe that gives the same pressure loss or resistance as the rectangular channel), and v is the average expected velocity through the window of the cell, g is the acceleration due to gravity, and f is the friction factor.

$$D_e = \frac{4wh}{2(w+h)} \qquad \text{(eqn. 4.3)}$$

The friction factor (f) is determined using the Reynolds number (R_e) for the desired velocity of flow and the relative roughness of the channel from the Moody chart (Moody 1944), a graph in non-dimensional form that relates the friction

factor, Reynolds number and relative roughness for a fully developed flow in a circular duct.

For the dimensions of the microfluidic channel in the *in-situ* flow cell device, the calculated flow rate is 24 µL/hr. The (200 x 80 x 1.5) µm sized micro-electrochemical cell cavity (a volume of 24000 μm^3) comprises $2.4x10^{-5}$ µL of electrolyte. The flow rate of 24 µL/hr converted using (1 µL = 10^9 μm^3, 1 hr = 3600 s) is $6.7x10^6$ μm^3/s. Thus, at the flow used, it takes ~4 s to replace all of the electrolyte in the cell compartment. In the immediate vicinity of the electrodes where the electrochemistry is taking place, the electrolyte exchange rate will be considerably faster. In the (30 x 25) µm area of the *in-situ* flow STXM study (Ch. 6), the electrolyte was changed every 0.2 s, a rate that is rapid compared to both the image acquisition rate (20 s/image) and the CV scan rate (10 mV/s).

Upon further experimental optimization of the flow rate it was found that a flow rate of 16-20 µL/hr provides a continuous and stable flow through the device under infuse (push) mode of the syringe pump. Using a flow rate below the optimized range, does not cause a failure but reduces the velocity of electrolyte in the device. However, a flow rate above the optimized range increases the resistance to flow and stops it completely. Prolonged pumping at a higher flow rate subsequently leads to build up of pressure between the chips (at the inlet port) and may cause leak of electrolyte from the edges of the chip.

CHAPTER 5.   *IN-SITU* STUDIES ON COPPER

ELECTRO-DEPOSITION AND ELECTRO-STRIPPING

This chapter presents results of an in-situ study of Copper (Cu) electro-deposition and electro-stripping. It discusses optimum design of in-situ electro-chemical STXM experiments, describes data collection and interpretation methods, and presents key findings on the Cu system based on the in-situ data.

5.1 Electrolyte

Electrodeposition and stripping of Cu was used to demonstrate the capabilities of the phase 1b *in-situ* flow electrochemical device. The chemicals used were all reagent grade; namely, copper sulphate pentahydrate, $CuSO_4.5H_2O$ (Sigma-aldrich, $\geq 98\%$), ammonium sulphate, $(NH_4)_2SO_4$ (Sigma-aldrich, $\geq 99\%$). A freshly prepared electrolyte of 10 mM $CuSO_4.5H_2O$ in 25 mM $(NH_4)_2SO_4$ (as supporting electrolyte) in milli-Q water, at a pH of 4.75 was used as a flowing electrolyte. A phase 1b electrochemical flow cell was assembled (see **section 4.3.2**) and mounted in the CLS a-STXM for *in-situ* experiments.

5.1.2 Protocol of in-situ electrochemical STXM

STXM has a slow acquisition rate, which is dependent on the user defined measurement parameters such as step size, dwell time, scan area, all of which affect the time for a measurement and quality of the resulting data. The user selects values for each of these parameters, depending on the scientific questions

being addressed. In this case, the chemical species present and changes in their quantitative spatial distribution as the reaction proceeds were of interest. A (30x25) μm scan area, 300 nm step size, 1 ms dwell time were selected, resulting in an acquisition time of ~20 s per image. Since the distribution of species was of interest a 3-energy image stack method was used with the energies selected [930.6eV **(A)**, 933.08eV **(B)**, and 937.05eV **(C)**] based on the absorption spectra of Cu(II), Cu(I) and Cu(0) species. (see **Figure 3.6a**).

The next experimental aspect to be designed is the cyclic voltammetry (CV) scan parameters; namely, start and end points, scan rate, and number of cycles. These parameters must be selected with the STXM image acquisition times in mind. The scan rate of the cyclic voltammetry determines the number of potential points at which an *in-situ* data are collected. In this case, a CV scan covering the Cu(I)-Cu(II) redox potentials, and providing *in-situ* data from 12 values of potential was achieved by running a 3 cycle CV scan for 780 s in total over a potential range of -500 mV to +150 mV, with a scan rate of 5 mV/s, using the Ivium pocketSTAT potentiostat (described in **section 2.3**).

5.2 Results and Discussion

5.2.1 Analysis and Interpretation of in-situ STXM Data

The measured 3-energy image stacks were aligned and converted to optical density (OD) images using the incident flux (I_0) spectra from regions of the stack area without deposited Cu species. Within each stack, the individual OD images at 930.6, 933.1 and 937.0 eV, referred to as OD_A, OD_B, and OD_C respectively are extracted. A 2-component stack fit of the stack was performed using Cu(0) and Cu(I) OD1 reference spectra. This results in Cu(I) and Cu(0) component maps and the constant image which is a map of electrode (**Figure 5.1**). A rescaled colour composite map was then assembled with the Cu(0) map in red, the Cu(I) in green, and the constant map (Au electrode) in blue. This gives a visual representation of the distribution of Cu(0) and Cu(I) species. Similar RGB maps generated from each of the *in-situ* image stack were then compiled as a movie with the frame rates synchronized with the CV curve, **Movie 1** (Prabu and Hitchcock 2017).

The current response in all 3 CV cycles (**Figure 5.2**) shows a shape typical of diffusion limited electrodeposition and electrostripping of Cu species (Williamson, Tromp et al. 2003). At +0.15 V, the start of the potential scan, the current is almost insignificant. When the potential has dropped to -0.2 V the charge required to overcome the Helmholtz double layer charge at the electrode

surface has been achieved. This is followed by a reduction peak current at ca. -0.31 V versus Au reference, which is comparable with the reduction peak potential reported in *in-situ* TEM studies of the same system (Williamson, Tromp et al. 2003).

Subsequently, upon reversing the direction of potential scan at -0.5 V, the current is low until a potential of ca. +0.05 V is reached, at which point there is a strong oxidation current. Another interesting observation from the CV curve is the crossover of the anodic and cathodic curves. This is due to the use of a Au electrode which has an entirely different microstructure compared to copper metal which causes a crystallographic substrate-metal misfit. This is also why the observed reduction potentials are larger than the standard reduction potentials of copper (Pletcher, Greff et al. 2010).
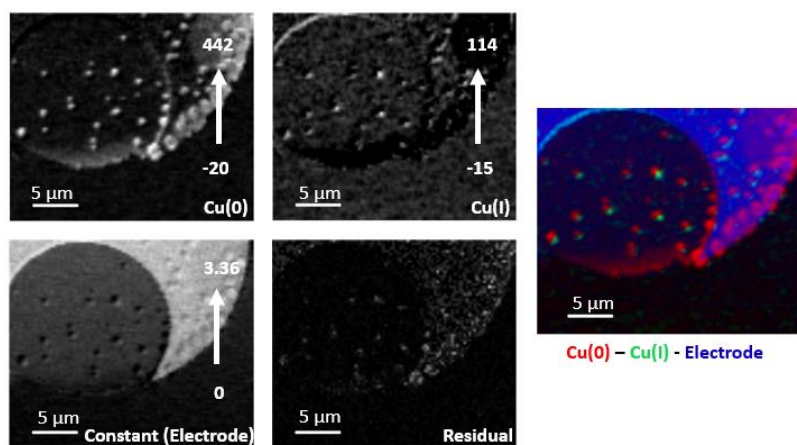
Figure 5.1 Component maps for Cu(I), Cu(0) and constant (electrode) and the RGB composite map resulting from stack fit to a Cu 2p stack.
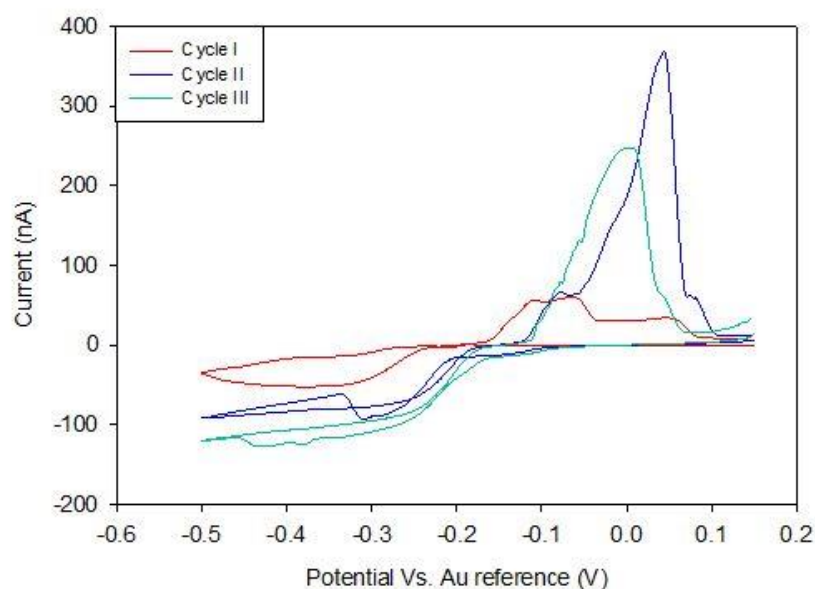
Figure 5.2 Cyclic voltammetric response during the *in-situ* experiment.

Figure 5.3 plots the current as a function of time for the 3-cycle potential scan and presents selected frames from the movie of the *in-situ* colour composite maps. Each color image is derived from STXM images at 3 different energies, with each image taking ~20 s to record. So, each color map averages electrochemical changes over a period of ~60 seconds, which spans a potential range of 300 mV. The potentials indicated in Fig **5.3** are the mean potential of the WE over the 60s time. Thus, each color map is an integrated representation of the electrochemical changes occurring over a potential range of $X \pm 150$ mV.
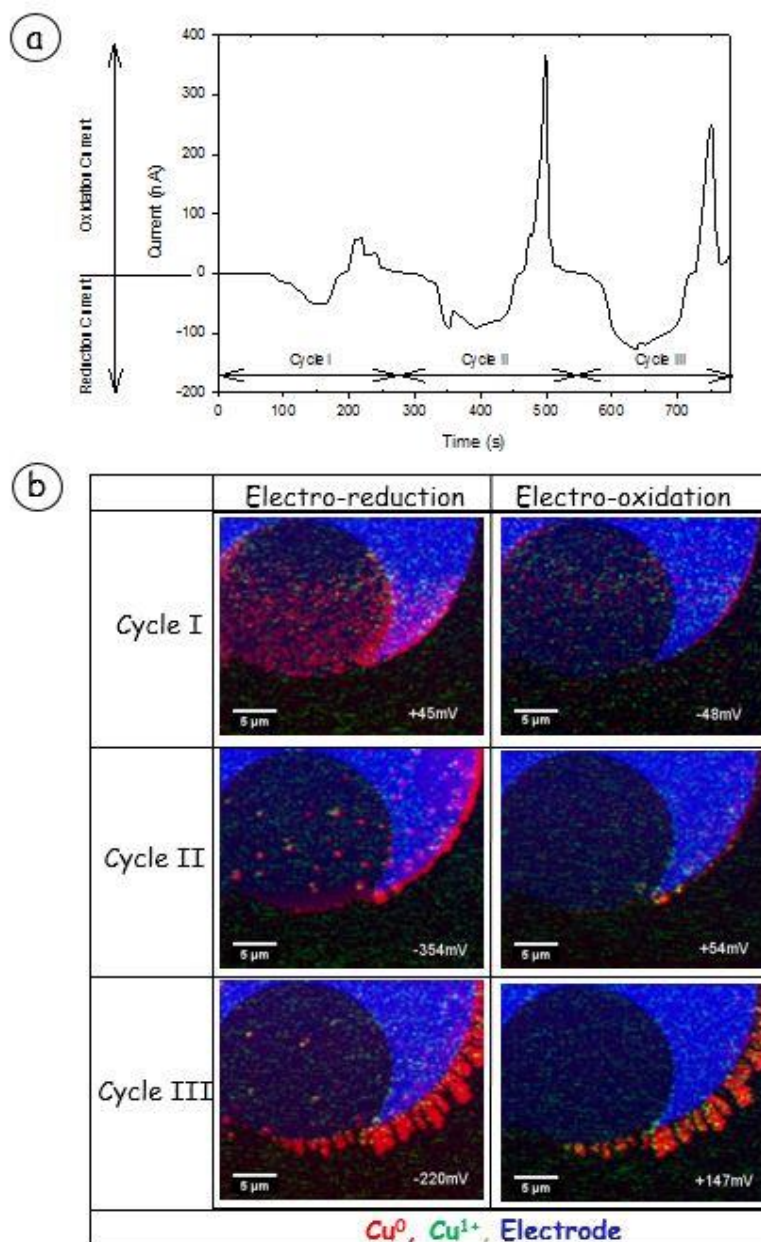
Figure 5.3 (a) I-t plot of the 3 cycle CV scan, (b) Colour coded maps
(red=Cu(0), green=Cu(I), blue=constant (electrode) for various points in the 3-
cycle CV scan.

The RGB maps in figure **5.2** are interpreted as follows. During cycle I of the CV, the first electrodeposition is observed in the potential range of. +45 mV ($\pm$150 mV), followed by subsequent electro-stripping at ca. -48 ($\pm$150) mV. In this cycle, the charge applied is used mainly for double layer charging. During this step, nucleation, and initial growth of Cu islands occurs both at the edge of the working electrode, and on the surface of the thin part of the electrode. There is much more deposition to the right of the electrode because that is the side facing the counter electrode. During cycle II of the CV experiment, electrodeposition and electro-stripping occur at potentials of -354 $\pm$150 mV and +54 $\pm$150 mV, respectively. The extensive deposition and large current signals seen in cycle II is associated with the presence of pre-deposited Cu nuclei which provide more active sites for electrodeposition and growth of the Cu deposits (Grujicic and Pesic 2002). During the stripping cycle, Cu metal at the edge of the electrode is stripped first which can interrupt the electrical connection to the dendritic features grown during cycle II and cycle III deposition. After disconnect, it is no longer possible to oxidatively strip the Cu in those dendrites which is then left behind in the electrolyte. Thus, by the end of the third cycle the process is clearly non-reversible. Further insights into the reversibility of Cu electrochemical system at these conditions are discussed in the following section.

5.2.2 Quantitative interpretation of in-situ STXM data

Cu(I) was observed only in the first cycle of CV. So only the Cu(0) species, was quantified using the method discussed in the next section. The maps from the *in-situ* data are quantitative due to the use of OD1 reference spectra in the fit. Threshold masks (map of components on a 0/1 z-scale) were then generated from the Cu(0) thickness maps in order to derive the average amounts of Cu(I) and Cu(0) at each pH condition.

Figure 5.4 represents a detailed graphical flow scheme of this data treatment process. After multiplying the threshold masks and the thickness data
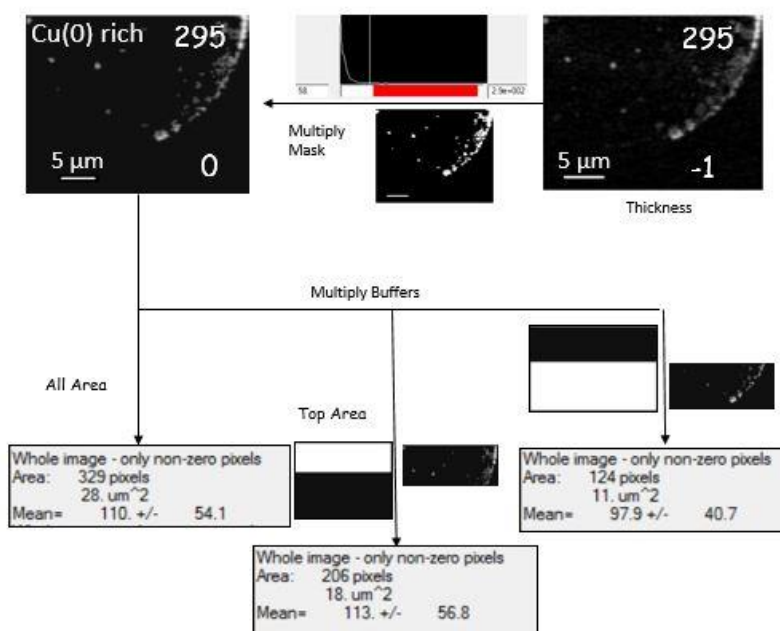
Figure 5.4 Flow scheme of data treatment process for quantification of the *in-situ* data.

from the Cu(0) rich component, the non-zero pixels were averaged to give the average thickness of the deposits.

To have a more precise representation of the uncertainties, similar threshold masks for two halves of the scan area were generated manually, followed by multiplication to thickness maps, and averaging of the thickness data for each species from each half of the measured area.

The resulting average thickness and area information were used to compute the amount (ng) of each component deposited, through conventional mass-density calculations using standard densities (see **section 3.4.3**). **Figure 5.5**
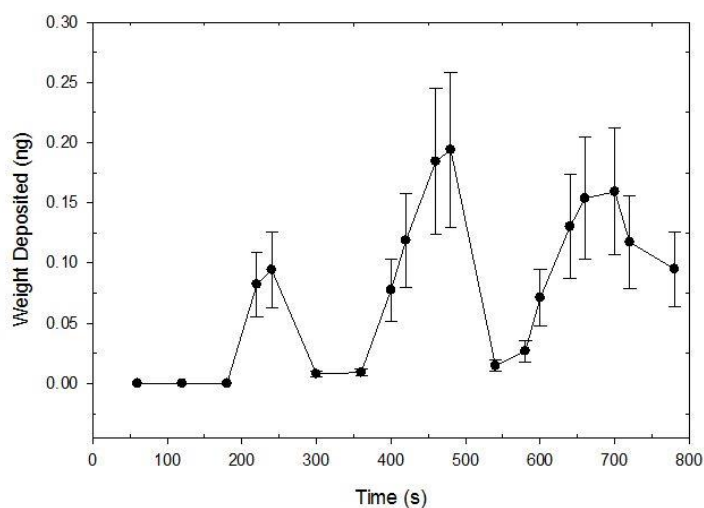
Figure 5.5 Quantitative representation of amount of Cu(0) deposited with respect to time during the CV experiment.
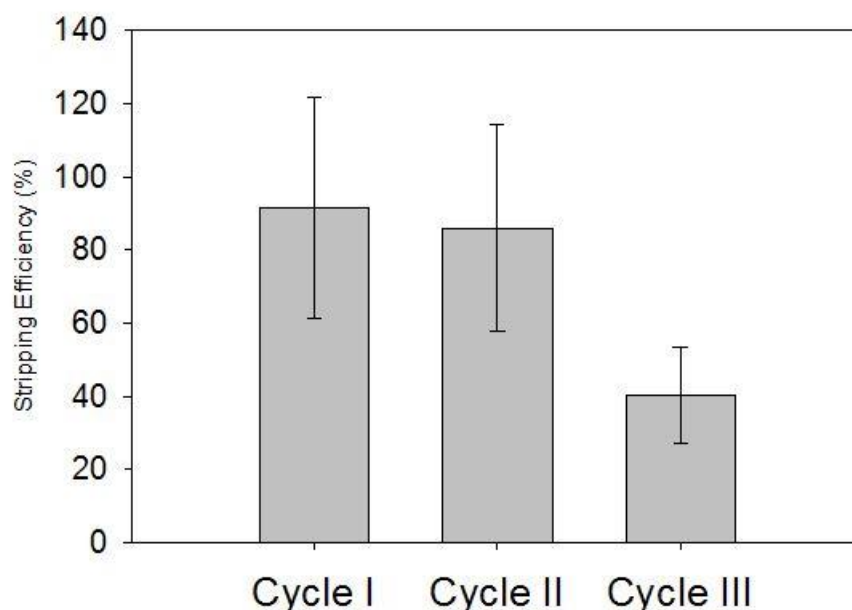
Figure 5.6 Bar chart presenting the stripping efficiency of Cu(0) at the end of each CV cycle.

presents the *in-situ* quantitative interpretation of the amount of Cu(0) deposited with respect to time during the CV experiment.

There is a sequential increase and decrease in the amounts of Cu(0) deposited with the shifts in reduction and oxidation potentials, respectively. The information on the amounts of Cu(0) at the end of reduction current and the oxidation current were used to compute the stripping efficiency/recyclability at the end of each cycle of CV (**Figure 5.6**).

Figure 5.3 shows that conformal and near-uniform films at the beginning of the CV experiment turn into rounded dendrites at the current densities passed

through the WE. Upon reversing the current, parts of the dendrites are left behind

in the electrolyte region which were no longer in electrical contact with the

electrode, leading to deterioration in the stripping efficiency (**Figure 5.6**).

Understanding the growth kinetics of such dendrites in copper electrochemical

systems is important in optimization of deposition process in manufacture of

semiconductor Cu interconnects as these dendrites are a cause of failure of a

device due to a break in the conductivity path (as affects this experiment) or by

electrical shorting (Gabrielli, Ostermann et al. 2003). Further *in-situ* STXM

studies on this system under a controlled-current deposition mode would help

identify current densities and other conditions that result in a conformal, pure Cu

metal deposit.

The deterioration of reversibility of the Cu electrochemical system studied

can be related to one of the common failure mechanism of Lithium ion batteries,

wherein the retention of such dendrites in the electrolyte, results in disproportional

lithiation and de-lithiation cycles under circumstances of overcharging or over-

discharging of the battery (Hendricks, Williard et al. 2015). This observation

suggests *in-situ* electrochemical STXM could be useful in battery research.

CHAPTER 6.   SUMMARY AND FUTURE WORK

This chapter summarizes the improvements achieved in in-situ flow electrochemical STXM and what was learnt from the in situ STXM studies of Cu electrodeposition. The present shortcomings of this instrument and proposals for future work to advance this technique are discussed.

6.1 Summary of thesis

This thesis has achieved a significant advance relative to previous *in-situ* electrochemical STXM studies (Guay, Stewart-Ornstein et al. 2005, Bozzini, Gianoncelli et al. 2014, Hitchcock, Qin et al. 2016, Lim, Li et al. 2016, Nagasaka, Ohigashi et al. 2017, Wu, Yin et al. 2017). Previous studies in our group were limited to spectroscopic and spatial investigations under non-flow conditions. While Bozzini and co-workers (Bozzini, Abyaneh et al. 2012), have performed *in situ* flow electrochemical studies, their analytical approach is primarily based on X-ray fluorescence detection which provides only elemental analysis, not the chemical speciation that NEXAFS provides. In my thesis, I measured and quantitatively analyzed results from both *in-situ* and *ex-situ* studies of Cu electrodeposition. The influence of pH on Cu electrochemistry in the presence and absence of IR drop was investigated and possible approaches to electrodeposition of Cu(I) from aqueous electrolyte were discussed.

While my thesis research has made considerable progress in developing *in-situ* flow electrochemical STXM instrumentation, there is still scope for further advancements, which are discussed below. These proposed improvements could enable studies of advanced electrochemical systems such as oxygen reduction half-cell reactions under conditions relevant to PEM-FC cathodes (which is the original motivation and target of the project), studies on mechanisms of corrosion of metals resulting in new technology for corrosion protection (Kurtis, Meyer-Ilse et al. 2000), or studies of redox flow batteries (Rhodri, Leon et al. 2016).

6.2 Future Work

6.2.1 Instrumental improvements

During *November 2016*, I attempted to operate the flow electrochemical device under high vacuum at the STXM on ALS beamline 11.0.2. This lead to an extensive leak of electrolyte which caused serious damage to the STXM optics. Post experiment analysis suggested two causes of this incident; firstly, the edges of the 'E' and 'F' silicon chips had not been sealed with epoxy. Despite my belief that the 'keeper' piece would apply sufficient pressure to create a seal, there was no seal at that spot. Secondly, I left the device overnight at the focal point of the microscope (and thus very close to the expensive Fresnel zone plate and other sensitive optics) with the syringe pump continuously driving electrolyte flow. This resulted in ~0.5 mL of acidic electrolyte (pH 1) being leaked into the STXM

which damaged the ZP, the upstream Si_3N_4 window, and several interferometry devices. Several improvements in instrumentation and operational protocol are recommended to avoid future occurrence of such incidents.

i.   All devices intended for operation in vacuum must be tested in a vacuum chamber equipped with a mass spectrometer to check for leaks.

ii.   If there is any concern of possible window breakage or leaks, the device should not be operated in vacuum, but rather the air in the STXM should be replaced with He without reducing the pressure, as was done in the successful experiments performed at the CLS a-STXM (in *October 2016* and *January 2017*).

iii. Whenever the *in-situ* flow device is not in use, or if there is a large change in flow conditions or potential, the device should be retracted at least 5 mm downstream from the focal point, thereby minimizing the damage that could occur in the unfortunate event of a leak.

As a consequence of this incident, ALS has now mandated that all STXM devices containing fluids must be able to sustain high vacuum without leaking. ALS is in the process of developing a test apparatus to verify this. In the case of the existing Phase 1b system, use of epoxy to fully seal the device may lead to compliance with this requirement.

In the longer term during the evolution of phase 2 of this project, advanced instrumentation and microfabrication techniques could be employed;

i.   A fully o-ring sealed device, such as those used at the UVSOR-STXM (Nagasaka, Ohigashi et al. 2017) or at Elettra (Bozzini, Gianoncelli et al. 2014) is one possibility.

ii.   Directly heat bond the two chips using a thin layer of suitable gasket material such as parylene-C (Temiz, Lovchik et al. 2015).

iii. Anodic bonding of the top and bottom chips during microfabrication stages. This will result in a hermetically sealed cell compartment suitable for direct mounting into the phase 1b holder (Masteika, Kowal et al. 2014).

The latter solution might work for Cu electrodeposition and similar electrochemical systems where the chemical reagents can be introduced by the fluid flow. However, it does not allow the user to introduce solid materials such as a microtomed section of a PEM-FC membrane electrode assembly, or to ink-jet print an experimental cathode on one of the electrodes. Those two methods are being considered as an approach for *in situ* flow studies of the oxygen reduction half-cell reaction. For such studies, as well as environmental electrochemical studies being performed by Dr. Martin Obst (Bayreuth) and Dr. Sarah Harmer

(Adelaide), who are part of a broader collaboration to develop this instrumentation, the ability to separate the two chips is an essential requirement.

The electrode material used in the present devices are 25 or 100 nm thick gold with a Ti-W adhesion layer. While it is possible to transform these electrodes into other materials (Cu, Pt, W, etc) by further layers of electrodeposition, this does not provide for cases where porous electrodes are needed, such as fuel cells and corrosion. Techniques for direct casting or printing of porous electrode surfaces are needed. My group is collaborating with Dr. Marc Secanell (University of Alberta) who has the facility to ink jet print PEM-FC cathodes with few micron precision. Developing this capability through collaboration would elevate the studies to the next level of probing electrochemical events in batteries, fuel cells, etc.

6.2.2 Future experiments

My research involved *ex-situ* STXM investigations at Cu 2p and O 1s edges, on the distribution of electrodeposited Cu(0) and Cu(I) species from an acidic aqueous electrolyte, in the presence and absence of Na_2SO_4 supporting electrolyte. This can be extended to (i) studies at S 2p edge for *ex-situ* STXM based investigations on the hypothesis of extensive adsorption of SO_4^{2-} on the electrode surface, and (ii) change of the supporting electrolyte to one without sulphate anions (e.g. sodium acetate). There is a recently reported technique

claiming to produce pure Cu_2O under slight acidic electrolyte conditions in a system of cupric acetate and sodium acetate (Charith, Vassilios et al. 2015). *Ex-situ* STXM studies could be extended to optimize the deposition conditions in this system.

At present, using STXM imaging to track electrochemical events over the entire electrode area is not yet feasible. However, smaller areas can be recorded more quickly, and tracking changes at a single position at 1 energy can be done in the sub-second time scale, as has been shown previously (Guay, Stewart-Ornstein et al. 2005). Even with the slow rate of acquisition achieved in this work, the ability to monitor changes in chemical states over space, time and applied potential gives added value relative to other *in situ* and *operando* electrochemical methods. Improvements in acquisition rate and spatial resolution would further improve this *in-situ* electrochemical STXM method. Although the phase 1b *in-situ* flow electrochemical STXM device is now established through my thesis studies, there is still scope for huge advancement. Phase 2 beckons.

Within the scope of the phase 1b system, the following ideas can be considered to further establish the capabilities of this technique:

i.   Experimental *in-situ* STXM studies comparing Cu electrodeposition under two electrolyte systems is of interest, such as $CuSO_4$ in NH_4SO_4 versus $Cu(CH_3COO)_2$ in CH_3COONa (Charith, Vassilios et al. 2015). The

influence of current density on the morphology of deposits and distribution of Cu(I) and Cu(0) species under different pH conditions is also of interest.

ii. *Ex-situ* STXM based investigations of the influence of IR drop compensation on Cu(I) stabilization comparing two cases: *(a)* using supporting electrolytes with SO_4^{2-} anions vs. *(b)* supporting electrolytes without SO_4^{2-} anions.

iii. Lab based numerical simulations of advanced electrode design for the phase 2 devices should be performed using tools such as COMSOL Multiphysics or ANSYS (Saias, Autebert et al. 2011, Scaramuzza, Ferrario et al. 2012). This could lead to a uniform field and current distribution over the WE area in contact with the electrolyte. This improvement could permit studies of the double layer of an electrochemical system.

iv. Exploration of techniques for surface modification of the phase 1b gold electrodes such as electrodeposition, spin-coating, or ink-jet printing. All potentials reported in the current *in-situ* research were with respect to the Au reference electrode. Modifying the RE surface by depositing a layer of silver (Ag) followed by drop casting $FeCl_3$ would allow *in-situ* measurement of potentials referenced to the standard Ag/AgCl electrode (Polk, Stelzenmuller et al. 2006).

REFERENCES

3DSystems.   from
https://www.3dsystems.com/sites/default/files/projet_3500_plastic_0115_usen_web.pdf.

Arimoto , S., D. Oyamatsu, T. Torimoto and S. Kuwabata (2008). "Development of In Situ Electrochemical Scanning Electron Microscopy with Ionic Liquids as Electrolytes." ChemPhysChem **9**(5): 763-767.

Attwood, D. (2007). Soft X-Rays and Extreme Ultraviolet Radiation: Principles and Applications, Cambridge University Press.

Bacskai, J., G. Inzelt, A. Bartl, L. Dunsch and G. Paasch (1994). "In situ electrochemical ESR investigations of the growth of one- and two-dimensional polypyrrole films." Synthetic Metals **67**(1): 227-230.

Bard, A. and L. Faulkner (2001). Electrochemical Methods: Fundamentals and Applications, John Wiley & Sons, Inc.

Bard, A., R. Parsons and J. Jordan (1985). Standard Potentials in Aqueous solution, CRC Press.

Bertrand, G., E. Rocca, C. Savall, C. Rapin, J. C. Labrune and P. Steinmetz (2000). "In-situ electrochemical atomic force microscopy studies of aqueous corrosion and inhibition of copper." Journal of Electroanalytical Chemistry **489**(1–2): 38-45.

BioLogic, S. I. "Small Volume Cell - 3 (SVC-3)." from http://www.bio-logic.net/en/accessories/analytical-cell-kit/small-volume-cells/?filter[division]=ec-lab.

Bozzini, B., M. K. Abyaneh, M. Amati, A. Gianoncelli, L. Gregoratti, B. Kaulich and M. Kiskinova (2012). "Soft X-ray Imaging and Spectromicroscopy: New Insights in Chemical State and Morphology of the Key Components in Operating Fuel-Cells." Chemistry – A European Journal **18**(33): 10196-10210.

Bozzini, B., M. Amati, L. Gregoratti, M. Kazemian, M. Prasciolu, E. Tondo, A. L. Trygub and M. Kiskinova (2012). "In Situ Electrochemical X-ray Spectromicroscopy Investigation of the Reduction/Reoxidation Dynamics of Ni–Cu Solid Oxide Fuel Cell Anodic Material in Contact with a Cr Interconnect in 2 $\times$ 10–6 mbar O_2." The Journal of Physical Chemistry C **116**(13): 7243-7248.

Bozzini, B., M. Amati, L. Gregoratti and M. Kiskinova (2013). "*In-situ* Photoelectron Microspectroscopy and Imaging of Electrochemical Processes at the Electrodes of a Self-driven Cell." Scientific Reports **3**: 2848.

Bozzini, B., M. Amati, L. Gregoratti, C. Mele, M. K. Abyaneh, M. Prasciolu and M. Kiskinova (2012). "*In-situ* photoelectron microspectroscopy during the operation of a single-chamber SOFC." Electrochemistry Communications **24**: 104-107.

Bozzini, B., A. Gianoncelli, P. Bocchetta, S. Dal Zilio and G. Kourousias (2014). "Fabrication of a Sealed Electrochemical Microcell for *in-situ* Soft X-ray Microspectroscopy and Testing with in Situ Co-Polypyrrole Composite Electrodeposition for Pt-Free Oxygen Electrocatalysis." Analytical Chemistry **86**(1): 664-670.

Bozzini, B., A. Gianoncelli, B. Kaulich, C. Mele, M. Prasciolu and M. Kiskinova (2013). "*In-Situ* Soft X-ray Microscopy Study of Fe Interconnect Corrosion in Ionic Liquid-Based Nano-PEMFC Half-Cells." Fuel Cells **13**(2): 196-202.

Bozzini, B., C. Mele, A. Gianoncelli, B. Kaulich, M. Kiskinova and M. Prasciolu (2011). "In situ X-ray spectromicroscopy study of bipolar plate material stability for nano-fuel-cells with ionic-liquid electrolyte." Microelectronic Engineering **88**(8): 2456-2458.

Breuer, N., A. M. Funtikov, U. Stimming and R. Vogel (1995). "In situ electrochemical STM imaging of roughened gold and platinum electrode surfaces." Surface Science **335**: 145-154.

Bruus, H. (2015). Chapter 1 Governing Equations in Microfluidics. Microscale Acoustofluidics, The Royal Society of Chemistry**:** 1-28.

Buckley, C., H. Rarback, R. Alforque, D. Shu, H. Ade, S. Hellman, N. Iskander, J. Kirz, S. Lindaas, I. Mcnulty, M. Oversluizen, E. Tang, D. Attwood, R. DiGennaro, M. Howells, C. Jacobsen, Y. Vladimirsky, S. Rothman, D. Kern and D. Sayre (1989). "Soft X-ray imaging with the 35 period undulator at the NSLS." Review of Scientific Instruments **60**(7): 2444-2447.

Charith, J., K. Vassilios, S. Withana and J. Sumedha (2015). "Improved efficiency of electrodeposited p-CuO-Cu$_2$O heterojunction solar cell." Applied Physics Express **8**(6): 065503.

Chen, J. G. (1997). "NEXAFS investigations of transition metal oxides, nitrides, carbides, sulfides and other interstitial compounds." Surface Science Reports **30**(1): 1-152.

Christensen, P. A., A. Hamnett and A. R. Hillman (1988). "An in-situ infra-red study of poly thiophene growth." Journal of Electroanalytical Chemistry and Interfacial Electrochemistry **242**(1): 47-62.

Ciobanu, M., J. P. Wilburn, M. L. Krim and D. E. Cliffel (2007). 1 - Fundamentals A2 - Zoski, Cynthia G. Handbook of Electrochemistry. Amsterdam, Elsevier**:** 3-29.

Ciobanu, M., J. P. Wilburn, M. L. Krim and D. E. Cliffel (2007). 1 - Fundamentals. Handbook of Electrochemistry. Amsterdam, Elsevier**:** 3-29.

Coffey, T., S. G. Urquhart and H. Ade (2002). "Characterization of the effects of soft X-ray irradiation on polymers." Journal of Electron Spectroscopy and Related Phenomena **122**(1): 65-78.

Compton, R. G. and A. M. Waller (1985). "An improved cell for in-situ electrochemical ESR." Journal of Electroanalytical Chemistry and Interfacial Electrochemistry **195**(2): 289-297.

Danilov, A. I., E. B. Molodkina, A. V. Rudnev, Y. M. Polukarov and J. M. Feliu (2005). "Kinetics of copper deposition on Pt(1 1 1) and Au(1 1 1) electrodes in solutions of different acidities." Electrochimica Acta **50**(25–26): 5032-5043.

de Jongh, P. E., D. Vanmaekelbergh and J. J. Kelly (1999). "Cu2O: Electrodeposition and Characterization." Chemistry of Materials **11**(12): 3512-3517.

Digby, D. M. (1977). Transient Techniques in Electrochemistry. New York, Plenum Press.

Fink, J., T. Müller-Heinzerling, B. Scheerer, W. Speier, F. U. Hillebrecht, J. C. Fuggle, J. Zaanen and G. A. Sawatzky (1985). "2p absorption spectra of the 3d elements." Physical Review B **32**(8): 4899-4904.

Gabrielli, C., E. Ostermann, H. Perrot and S. Mege (2003). "Post-copper CMP cleaning galvanic phenomenon investigated by EIS." Proceedings-Electrochemical Society **26**: 321-328.

Genies, E. M., G. Bidan and A. F. Diaz (1983). "Spectroelectrochemical study of polypyrrole films." Journal of Electroanalytical Chemistry and Interfacial Electrochemistry **149**(1): 101-113.

Geniès, E. M. and P. Noël (1991). "Synthesis and polymerization of o-hexylaniline." Journal of Electroanalytical Chemistry and Interfacial Electrochemistry **310**(1): 89-111.

Gianoncelli, A., B. Kaulich, M. Kiskinova, M. Prasciolu, B. D. Urzo and B. Bozzini (2011). "An in situ electrochemical soft X-ray spectromicroscopy investigation of Fe galvanically coupled to Au." Micron **42**(4): 342-347.

Gorlin, Y., B. Lassalle-Kaiser, J. D. Benck, S. Gul, S. M. Webb, V. K. Yachandra, J. Yano and T. F. Jaramillo (2013). "In Situ X-ray Absorption Spectroscopy Investigation of a Bifunctional Manganese Oxide Catalyst with High Activity for Electrochemical Water Oxidation and Oxygen Reduction." Journal of the American Chemical Society **135**(23): 8525-8534.

Grioni, M., J. B. Goedkoop, R. Schoorl, F. M. F. de Groot, J. C. Fuggle, F. Schäfers, E. E. Koch, G. Rossi, J. M. Esteva and R. C. Karnatak (1989). "Studies of copper valence states with Cu-L3 X-ray absorption spectroscopy." Physical Review B **39**(3): 1541-1545.

Grioni, M., J. F. Van Acker, M. T. Czyžyk and J. C. Fuggle (1992). "Unoccupied electronic structure and core-hole effects in the x-ray-absorption spectra of Cu_2O." Physical Review B **45**(7): 3309-3318.

Grogan, J. M. and H. H. Bau (2010). "The Nanoaquarium: A Platform for *in-situ* Transmission Electron Microscopy in Liquid Media." Journal of Microelectromechanical Systems **19**(4): 885-894.

Grogan, J. M., H. H. Bau, J. Park, X. Ye, C. B. Murray and F. M. Ross (2012). "Liquid Cell *in-situ* Electron Microscopy: Interfacial Phenomena and Electrochemical Deposition." Microscopy and Microanalysis **18**(S2): 1160-1161.

Grogan, J. M., L. Rotkina and H. H. Bau (2011). "In situ liquid-cell electron microscopy of colloid aggregation and growth dynamics." Physical Review E **83**(6): 061405.

Grujicic, D. and B. Pesic (2002). "Electrodeposition of copper: the nucleation mechanisms." Electrochimica Acta **47**(18): 2901-2912.

Guay, D., J. Stewart-Ornstein, X. Zhang and A. P. Hitchcock (2005). "*In-situ* Spatial and Time-Resolved Studies of Electrochemical Reactions by Scanning Transmission X-ray Microscopy." Analytical Chemistry **77**(11): 3479-3487.

Hahner, G. (2006). "Near edge X-ray absorption fine structure spectroscopy as a tool to probe electronic and structural properties of thin organic films and liquids." Chemical Society Reviews **35**(12): 1244-1255.

Hendricks, C., N. Williard, S. Mathew and M. Pecht (2015). "A failure modes, mechanisms, and effects analysis (FMMEA) of lithium-ion batteries." Journal of Power Sources **297**: 113-120.

Henke, B. L., E. M. Gullikson and J. C. Davis (1993). "X-Ray Interactions: Photoabsorption, Scattering, Transmission, and Reflection at E = 50-30,000 eV, Z = 1-92." Atomic Data and Nuclear Data Tables **54**(2): 181-342.

Hillman, A. R., D. C. Loveday, D. E. Moffatt and J. Maher (1992). "Faraday communications. In situ electron paramagnetic resonance spectra of n- and p-doped poly(benzo[c]thiophene) films." Journal of the Chemical Society, Faraday Transactions **88**(22): 3383-3384.

Hitchcock, A. P. (2012). Soft X-Ray Imaging and Spectromicroscopy. Handbook of Nanoscopy, Wiley-VCH Verlag GmbH & Co. KGaA**:** 745-791.

Hitchcock,   A.   P.   (2016).   "aXis2000."   from http://unicorn.mcmaster.ca/aXis2000.html.

Hitchcock, A. P., Z. Qin, S. M. Rosendahl, V. Lee, M. Reynolds and H. Hosseinkhannazer (2016). "Electro-deposition of Cu studied with in situ electrochemical scanning transmission x-ray microscopy." AIP Conference Proceedings **1696**(1): 020003.

Horng-Show, K., W. Der-Tsuey, Y. Yi-Kuei, H. Shao-Hung, J. Jia-Yu, C. Mi and T. Ming-Fong (2012). "Effect of Cu_2O Doping in TiO_2 Films on Device Performance of Dye-Sensitized Solar Cells." Japanese Journal of Applied Physics **51**(10S): 10NE18.

Hossain, M. A., R. Al-Gaashani, H. Hamoudi, M. J. Al Marri, I. A. Hussein, A. Belaidi, B. A. Merzougui, F. H. Alharbi and N. Tabet (2017). "Controlled growth of Cu_2O thin films by electrodeposition approach." Materials Science in Semiconductor Processing **63**: 203-211.

Howells, M., C. Jacobsen, T. Warwick and A. Van den Bos (2007). Principles and Applications of Zone Plate X-Ray Microscopes. Science of Microscopy. P. W. Hawkes and J. C. H. Spence. New York, NY, Springer New York**:** 835-926.

Hulbert, S. L., B. A. Bunker, F. C. Brown and P. Pianetta (1984). "Copper L-2,3 near-edge structure in Cu_2O." Physical Review B **30**(4): 2120-2126.

Ivium Technologies, B. V. "IviumSoft^{TM}."

Ivium Technologies, B. V. "pocketSTAT: Handheld potentiostat/galvanostat/ZRA with integrated impedance analyser." from http://www.ivium.nl/pocketStat.

Ivium Technologies, B. V. (2017) "IviumSoft^{TM} Manual ".

Jacobsen, V., S. Wirick, G. Flynn and C. Zimba (2000). "Soft X-ray spectroscopy from image sequences with sub-100 nm spatial resolution." Journal of Microscopy **197**(2): 173-184.

Janos, K. and R. Harvey (1985). "Soft X-ray microscopes." Review of Scientific Instruments **56**(1): 1-13.

Jiang, P., J. L. Chen, F. Borondics, P. A. Glans, M. W. West, C. L. Chang, M. Salmeron and J. Guo (2010). "*In-situ* soft X-ray absorption spectroscopy investigation of electrochemical corrosion of copper in aqueous $NaHCO_3$ solution." Electrochemistry Communications **12**(6): 820-822.

John, O. M., A. Reddy and M. Gamboa-Aldeco (2001). Modern Electrochemistry 2A: Fundamentals of Electrodics, Springer.

Kato, H., O. Nishikawa, T. Matsui, S. Honma and H. Kokado (1991). "Fourier transform infrared spectroscopy study of conducting polymer polypyrrole: higher order structure of electrochemically-synthesized film." The Journal of Physical Chemistry **95**(15): 6014-6016.

Kilcoyne, A. L. D., T. Tyliszczak, W. F. Steele, S. Fakra, A. P. Hitchcock, K. Franck, E. Anderson, B. Harteneck, E. G. Rightor, G. E. Mitchell, L. Yang, T. Warwick and H. Ade (2003). "Interferometer-controlled scanning transmission X-ray microscopes at the Advanced Light Source." Journal of Synchrotron Radiation **10**(2): 125-136.

Kim, Y. T., R. W. Collins, K. Vedam and D. L. Allara (1991). "Real Time Spectroscopic Ellipsometry: In Situ Characterization of Pyrrole

Electropolymerization." Journal of The Electrochemical Society **138**(11): 3266-3275.

Kurtis, K. E., W. Meyer-Ilse and P. J. M. Monteiro (2000). "Soft X-ray spectromicroscopy for in situ study of corrosion." Corrosion Science **42**(8): 1327-1336.

Kuwabata, S., H. Yoneyama and H. Tamura (1984). "Redox Behavior and Electrochromic Properties of Polypyrrole Films in Aqueous Solutions." Bulletin of the Chemical Society of Japan **57**(8): 2247-2253.

Lambert, J. H. (1760). Photometria: Sive de Mensura et Gradibus Luminis, Colorum et Umbrae.

Lankinen, E., G. Sundholm, P. Talonen, T. Laitinen and T. Saario (1998). "Characterization of a poly(3-methyl thiophene) film by an in-situ dc resistance measurement technique and *in-situ* FTIR spectroelectrochemistry." Journal of Electroanalytical Chemistry **447**(1–2): 135-145.

Lapkowski, M. and E. M. Geniés (1990). "Evidence of two kinds of spin in polyaniline from in situ EPR and electrochemistry." Journal of Electroanalytical Chemistry and Interfacial Electrochemistry **279**(1): 157-168.

Lim, J., Y. Li, D. H. Alsem, H. So, S. C. Lee, P. Bai, D. A. Cogswell, X. Liu, N. Jin, Y. S. Yu, N. J. Salmon, D. A. Shapiro, M. Z. Bazant, T. Tyliszczak and W. C. Chueh (2016). "Origin and hysteresis of lithium compositional spatiodynamics within battery primary particles." Science **353**(6299): 566-571.

Madelung, O., U. Rössler and M. Schulz (1998). Cuprous oxide (Cu2O) Debye temperature, density, melting point: Datasheet from Landolt-Börnstein - Group III Condensed Matter · Volume 41C: "Non-Tetrahedrally Bonded Elements and Binary Compounds I" in SpringerMaterials (http://dx.doi.org/10.1007/10681727_60), Springer-Verlag Berlin Heidelberg.

Masteika, V., J. Kowal, N. S. J. Braithwaite and T. Rogers (2014). "A Review of Hydrophilic Silicon Wafer Bonding." ECS Journal of Solid State Science and Technology **3**(4): Q42-Q54.

Mills, D. M., J. R. Helliwell, A. Kvick, T. Ohta, I. A. Robinson and A. Authier (2005). "Report of the Working Group on Synchrotron Radiation Nomenclature - brightness, spectral brightness or brilliance?" Journal of Synchrotron Radiation **12**(3): 385.

Mobilio, S., F. Boscherini and C. Meneghini (2015). Synchrotron Radiation Basics, Methods and Applications, Springer Berlin Heidelberg.

Moody, L. F. (1944). "Friction Factors for Pipe Flow." Transactions of the ASME **66**(8): 14.

Morehouse, R. J. and B. L. Burris (1978). Catalog of National Bureau of Standards publications, 1966-1976. Washington, The Bureau : for sale by the Supt. of Docs., U.S. Govt. Print. Off.

Nagasaka, M., T. Hatsui, T. Horigome, Y. Hamamura and N. Kosugi (2010). "Development of a liquid flow cell to measure soft X-ray absorption in transmission mode: A test for liquid water." Journal of Electron Spectroscopy and Related Phenomena **177**(2–3): 130-134.

Nagasaka, M., T. Ohigashi and N. Kosugi (2017). "Development of In-Situ/Operando Sample Cells for Soft X-ray Transmission Spectromicroscopy at UVSOR-III Synchrotron." Synchrotron Radiation News **30**(2): 3-7.

Nakai, S. I., T. Mitsuishi, H. Sugawara, H. Maezawa, T. Matsukawa, S. Mitani, K. Yamasaki and T. Fujikawa (1987). "Oxygen K x-ray-absorption near-edge structure of alkaline-earth-metal and 3d-transition-metal oxides." Physical Review B **36**(17): 9241-9246.

Neugebauer, H. (1995). "In situ vibrational spectroscopy of conducting polymer electrodes." Macromolecular Symposia **94**(1): 61-73.

Norcada. "A MEMS Technology Company." from http://www.norcada.com/.

Pletcher, D., R. Greff, R. Peat, L. M. Peter and J. Robinson (2010). 2 - Steady state and potential step techniques. Instrumental Methods in Electrochemistry, Woodhead Publishing**:** 42-75.

Polk, B. J., A. Stelzenmuller, G. Mijares, W. MacCrehan and M. Gaitan (2006). "Ag/AgCl microelectrodes with improved stability for microfluidics." Sensors and Actuators B: Chemical **114**(1): 239-247.

Pompa, M., C. Li, A. Bianconi, A. Congiu Castellano, S. Della Longa, A. M. Flank, P. Lagarde and D. Udron (1991). "Full multiple scattering analysis of linearly polarized Cu L3-edge XANES of La_2CuO_4." Physica C: Superconductivity **184**(1): 51-64.

Prabu, V. and A. P. Hitchcock. (2017). "In-situ copper electrodeposition and electrostripping movie." from http://unicorn.mcmaster.ca/highlights/in_situ-flow-echem%20STXM/in_situ-flow-echem-stxm.html.

Rahman, A. S. M. S., M. A. Islam and K. M. Shorowordi (2015). "Electrodeposition and Characterization of Copper Oxide Thin Films for Solar cell Applications." Procedia Engineering **105**: 679-685.

Rarback, H., D. Shu, S. C. Feng, H. Ade, J. Kirz, I. McNulty, D. P. Kern, T. H. P. Chang, Y. Vladimirsky, N. Iskander, D. Attwood, K. McQuaid and S. Rothman (1988). "Scanning X-ray microscope with 75 nm resolution." Review of Scientific Instruments **59**(1): 52-59.

Rhodri, J., D. B. Leon, P. N. Tobias, M. Jason, P. F. Donal, M. M. H. Thomas, J. L. B. Dan and R. S. Paul (2016). "Design of a miniature flow cell for in situ x-ray imaging of redox flow batteries." Journal of Physics D: Applied Physics **49**(43): 434002.

Saias, L., J. Autebert, L. Malaquin and J. L. Viovy (2011). "Design, modeling and characterization of microfluidic architectures for high flow rate, small footprint microfluidic systems." Lab Chip **11**(5): 822-832.

Scaramuzza, M., A. Ferrario, E. Pasqualotto and A. De Toni (2012). "Development of an Electrode/Electrolyte Interface Model Based on Pseudo-Distributed Elements Combining COMSOL, MATLAB and HSPICE." Procedia Chemistry **6**: 69-78.

Soares, D. M., S. Wasle, K. G. Weil and K. Doblhofer (2002). "Copper ion reduction catalyzed by chloride ions." Journal of Electroanalytical Chemistry **532**(1–2): 353-358.

Souto, R. M., Y. González-García, D. Battistel and S. Daniele (2012). "In Situ Scanning Electrochemical Microscopy (SECM) Detection of Metal Dissolution during Zinc Corrosion by Means of Mercury Sphere-Cap Microelectrode Tips." Chemistry – A European Journal **18**(1): 230-236.

Stöhr, J. (1992). NEXAFS Spectroscopy. New York, Springer-Verlag Berlin Heidelberg.

Temiz, Y., R. D. Lovchik, G. V. Kaigala and E. Delamarche (2015). "Lab-on-a-chip devices: How to close and plug the lab?" Microelectronic Engineering **132**: 156-175.

Tjeng, L. H., C. T. Chen and S. W. Cheong (1992). "Comparative soft-x-ray resonant-photoemission study on $Bi_2Sr_2CaCu_2O_8$, CuO, and Cu_2O." Physical Review B **45**(14): 8205-8208.

Todd, E. C. and D. M. Sherman (2003). "Surface oxidation of chalcocite (Cu2S) under aqueous (pH=2-11) and ambient atmospheric conditions." American Mineralogist **88**(11-12): 1652-1656.

Tröger, L., T. Yokoyama, D. Arvanitis, T. Lederer, M. Tischer and K. Baberschke (1994). "Determination of bond lengths, atomic mean-square relative displacements, and local thermal expansion by means of soft-x-ray photoabsorption." Physical Review B **49**(2): 888-903.

Visijet. from http://infocenter.3dsystems.com/materials/sites/default/files/sds-files/professional/24184-s12-02-asds_ghsenglishvisijet_ex_200_and_crystal.pdf.

Volta, A. (1800). "On the Electricity Excited by the Mere Contact of Conducting Substances of Different Kinds. In a Letter from Mr. Alexander Volta, F. R. S. Professor of Natural Philosophy in the University of Pavia, to the Rt. Hon. Sir Joseph Banks, Bart. K. B. P. R. S." Philosophical Transactions of the Royal Society of London **90**: 403-431.

Wang, L., J. Kowalik, B. Mizaikoff and C. Kranz (2010). "Combining Scanning Electrochemical Microscopy with Infrared Attenuated Total Reflection Spectroscopy for in Situ Studies of Electrochemically Induced Processes." Analytical Chemistry **82**(8): 3139-3145.

Wang, P., H. Wu, Y. Tang, R. Amal and Y. H. Ng (2015). "Electrodeposited Cu_2O as Photoelectrodes with Controllable Conductivity Type for Solar Energy Conversion." The Journal of Physical Chemistry C **119**(47): 26275-26282.

Warwick, T., H. Ade, D. Kilcoyne, M. Kritscher, T. Tylisczcak, S. Fakra, A. P. Hitchcock, P. Hitchcock and H. Padmore (2002). "A new bend-magnet beamline for scanning transmission X-ray microscopy at the Advanced Light Source." Journal of Synchrotron Radiation **9**(4): 254-257.

White, F. (2008). Fluid mechanics, McGraw-Hill.

Wieckowski, A., P. Zelenay and K. Varga (1991). "A comprehensive study of bisulfate adsorption on Pt(111) by radioactive labeling and voltammetry." J. Chim. Phys. **88**: 1247-1270.

Williams, G. P. (1982). "A general review of synchrotron radiation, its uses and special technologies." Vacuum **32**(6): 333-345.

Williamson, M. J., R. M. Tromp, P. M. Vereecken, R. Hull and F. M. Ross (2003). "Dynamic microscopy of nanoscale cluster growth at the solid-liquid interface." Nat Mater **2**(8): 532-536.

Wu, S., Z. Yin, Q. He, G. Lu, Q. Yan and H. Zhang (2011). "Nucleation Mechanism of Electrochemical Deposition of Cu on Reduced Graphene Oxide Electrodes." The Journal of Physical Chemistry C **115**(32): 15973-15979.

Wu, Y. A., Z. Yin, M. Farmand, Y. S. Yu, D. A. Shapiro, H. G. Liao, W. I. Liang, Y. H. Chu and H. Zheng (2017). "In-situ Multimodal Imaging and Spectroscopy of Mg Electrodeposition at Electrode-Electrolyte Interfaces." **7**: 42527.

Zhao, W., W. Fu, H. Yang, C. Tian, M. Li, Y. Li, L. Zhang, Y. Sui, X. Zhou, H. Chen and G. Zou (2011). "Electrodeposition of Cu_2O films and their photoelectrochemical properties." CrystEngComm **13**(8): 2871-2877.

Zotti, G. and G. Schiavon (1989). "The polythiophene puzzle. Electrochemical and spectroelectrochemical evidence for two oxidation levels." Synthetic Metals **31**(3): 347-357.